# CANARDS UNDERLIE BOTH ELECTRICAL AND $Ca^{2+}$-INDUCED EARLY AFTERDEPOLARIZATIONS IN A MODEL FOR CARDIAC MYOCYTES *

JOSHUA KIMREY†, THEODORE VO‡, AND RICHARD BERTRAM§

**Abstract.** Early afterdepolarizations (EADs) are voltage oscillations that can occur during the plateau phase of a cardiac action potential. EADs at the cellular level have been linked to potentially deadly tissue-level arrhythmias and the mechanisms for their arisal are not fully understood. There is ongoing debate as to which is the predominant biophysical mechanism of EAD production: imbalanced interactions between voltage-gated transmembrane currents *or* over-active $Ca^{2+}$-dependent transmembrane currents brought about by pathological intracellular $Ca^{2+}$ release dynamics. In this article, we address this issue using a foundational 10-dimensional biophysical ventricular action potential model which contains both electrical and intracellular $Ca^{2+}$ components. Surprisingly, we find that the model can produce EADs through both *biophysical* mechanisms, which hints at a more fundamental *dynamical* mechanism for EAD production. Fast-slow analysis reveals EADs, in both cases, to be canard-induced mixed-mode oscillations. While the voltage-driven EADs arise from a fast-slow problem with two slow variables, the $Ca^{2+}$-driven EADs arise from the addition of a third slow variable. Hence, we adapt existing computational methods in order to compute 2D slow manifolds and 1D canard orbits in the reduced 7D model from which voltage-driven EADs arise. Further, we extend these computational methods in order to compute, for the first time, 2D sets of maximal canards which partition the 3D slow manifolds of the 8D problem from which $Ca^{2+}$-driven EADs arise. The canard viewpoint provides a unifying alternative to the voltage- or $Ca^{2+}$-driven viewpoints while also providing explanatory and predictive insights that cannot be obtained through the use of the traditional fast-slow approach.

**Key words.** excitable media, early afterdepolarizations, mixed-mode oscillations, canards, cardiac, numerical continuation

**AMS subject classifications.** 37N25, 92B05

## 1. Introduction.

Early afterdepolarizations (EADs) are pathological fluctuations in the membrane potential that can occur during cardiac action potentials [6] (see Fig. 1). These can greatly extend the action potential (AP) duration, and are associated with tachycardia (unusually fast heart rate) and sudden death [52, 56]. Studies with isolated cardiomyocytes have shown that EADs can be induced in a number of ways, including hypokalemic environments [28, 39, 40, 57] (i.e., environments with unusually low potassium levels), addition of $I_K$ channel blockers such as cesium ($Cs^+$) [1, 35, 36], and application of anti-arrhythmic drugs such as azimilide [59, 60] and E-4031 [37, 47]. Thus, the abnormal oscillations are produced by factors intrinsic to a single myocyte, and are not a network effect.

While it is clear that isolated myocytes can produce EADs, it is not so clear why they produce them. Are these abnormal oscillations in the membrane potential due to the nonlinear interactions of the ionic currents, or are they a product of the intracellular $Ca^{2+}$ dynamics? Both explanations are feasible, and in fact, there is evidence supporting both mechanisms. A classic study of the role $Ca^{2+}$ plays in EAD production found that existent EADs could persist despite the use of either $Ca^{2+}$-

*Submitted to the editors March 12, 2021.

**Funding:** This work was funded by the National Science Foundation, award number DMS 1853342 to T. Vo and R. Bertram

†Department of Mathematics, Florida State University, Tallahassee, FL 32306 (jkimrey@math.fsu.edu).

‡School of Mathematics, Monash University, Clayton, Australia (theodore.vo@monash.edu).

§Department of Mathematics, and Programs in Neuroscience and Biophysics, Florida State University, Tallahassee, FL 32306 (bertram@math.fsu.edu).

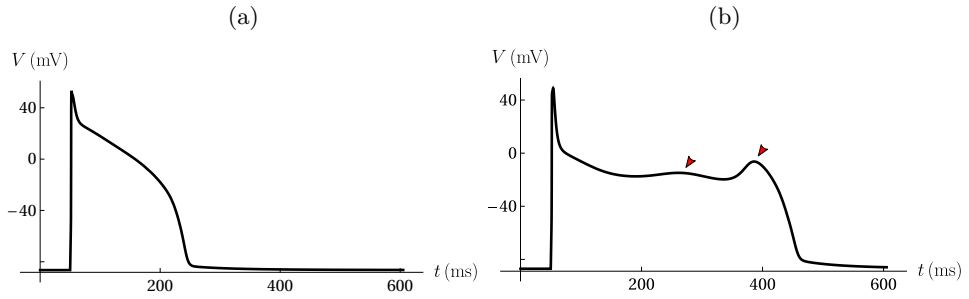


Fig. 1: **Standard AP morphology versus an AP with EADs.** (a) A standard AP is generated under standard conditions. (b) An AP with two EADs is generated under $Ca^{2+}$ overload conditions.

induced $Ca^{2+}$ release (CICR) antagonists—which bind to and inactivate intracellular $Ca^{2+}$ channels—or $Ca^{2+}$ chelators—which bind to intracellular $Ca^{2+}$ signaling ions [35]. A series of more recent studies used the dynamic clamp technique to induce EADs in the presence of the $Ca^{2+}$ channel blocker nifedipine. The inward $Ca^{2+}$ current was added back using the dynamic clamp, which uses a mathematical model to determine the current based on the cell's membrane potential. Though the current is added back, there is no influx of $Ca^{2+}$ ions, so the dynamics in intracellular $Ca^{2+}$ concentration ($[Ca^{2+}]_i$) had to be simulated in order to reconstruct physiological APs. The authors found that when the overlap region between the $Ca^{2+}$ current activation and inactivation (the so-called "$Ca^{2+}$ window current") was sufficiently wide and EADs were produced, the intracellular $Ca^{2+}$ dynamics passively followed, rather than led, the EAD-laden electrical dynamics [19,34]. These studies provide strong evidence for a class of EADs that are voltage-driven. Alternatively, other studies have shown that some EADs can be eliminated when CICR from the sarcoplasmic reticulum (SR) is inhibited [41,61] or when $Ca^{2+}$ chelators are added to the bathing solution [14,15]. These studies provide strong evidence for a $Ca^{2+}$-driven mechanism for EADs.

From a biophysical viewpoint then, there appear to be at least two mechanisms for EAD production. If, however, one examines the underlying dynamics behind each of these, it may be possible that the explanation is the same. That is, there may be one *dynamical explanation* for the very different *biophysical mechanisms*. Indeed, there are precedents for this, such as the mathematical description of $Ca^{2+}$ oscillations due to $Ca^{2+}$ release from the endoplasmic reticulum recast using similar equations to those for the generation of tonic action potentials [29]. The biophysics is entirely different, but the mathematical explanation is the same.

We explore this possibility here, using a mathematical model for ventricular myocytes that has components for electrical activity and intracellular $Ca^{2+}$ dynamics, and is capable of generating APs that exhibit EADs. We show that, in some cases, the EADs can be produced without active participation from the $Ca^{2+}$ module (i.e., $[Ca^{2+}]_i$ is clamped), but this is conditioned on the value of the $Ca^{2+}$ concentration. In other cases, the $Ca^{2+}$ dynamics are essential for the EAD production. Yet, in both cases, the explanation is the same from a dynamical viewpoint: the EADs are due to canards induced by folded node singularities. We demonstrate this point using

fast-slow analysis, and use this type of analysis to explain the influence of EAD-inducing and EAD-inhibiting pharmacological manipulations. This work builds on prior mathematical work from our group and others [2, 22, 23, 26, 53], but for the first time provides a unified explanation for both purely voltage-dependent EADs and those that also require $Ca^{2+}$ dynamics.

**2. The Luo-Rudy II Model.** The Luo-Rudy II model (LRII) of the guinea pig ventricular myocyte [31] was developed to account for emerging evidence of the prominent role played by intracellular $Ca^{2+}$ dynamics in regulating mammalian cardiac cell electrical activity. Many of the more detailed ventricular myocyte models that have emerged in the years since retain significant portions of the original formulations from [31]. Therefore, we analyze the Luo-Rudy II model for its ability to reproduce myriad experimental findings, for its added biophysical detail compared to Luo-Rudy I [30] (it includes prominent $Ca^{2+}$-dependent currents, such as the $Na^+$-$Ca^{2+}$ exchanger, and a more complete description of intracellular $[Ca^{2+}]_i$ dynamics), and for its analytical tractability. A summary schematic of the model cell with delineated voltage- and $Ca^{2+}$-module constituents is shown in Fig. 2.

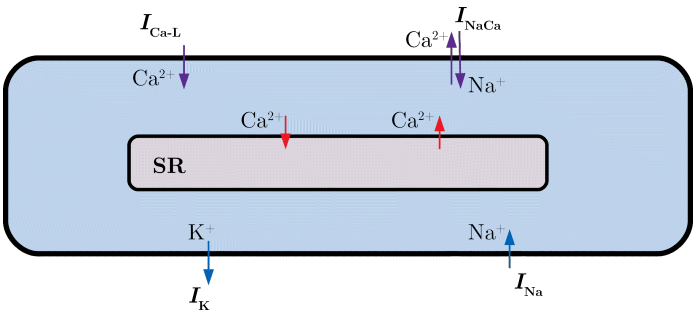


Fig. 2: **Summary schematic diagram of the Luo-Rudy II model.** The semi-separable electrical and $Ca^{2+}$modules are color-coded. Blue arrows denote transmembrane currents that belong strictly to the electrical module. Red arrows denote fluxes belonging to the $Ca^{2+}$ module. Purple arrows denote $Ca^{2+}$-dependent transmembrane currents that couple the electrical and $Ca^{2+}$ modules. The light blue and red spaces denote the myoplasm and the sarcoplasmic reticulum (SR), respectively.

To investigate the role that $Ca^{2+}$ dynamics play in the emergence and properties of EADs in the Luo-Rudy II model, three variants of the model are analyzed. Detailed model equations and parameters are provided in Appendix A. The first model variant excludes $Ca^{2+}$ dynamics and takes the form:

$$\begin{aligned} C_m \frac{\mathrm{d}V}{\mathrm{d}t} &= -\sum I_{\text{ion}} + I_{\text{stim}} \\ \frac{\mathrm{d}y}{\mathrm{d}t} &= \frac{y_\infty(V) - y}{\tau_y(V)}, \quad y = \{m, h, j, d, f, x\} \end{aligned} \tag{2.1}$$

where $C_m$ is membrane capacitance ($= 1\ \mu\mathrm{F/cm^2}$), $I_{\text{ion}}$ is the sum of 11 ionic currents which contain 6 dynamic variables, and $I_{\text{stim}}$ is a brief pulse of current with 30 $\mu\mathrm{A/cm^2}$ amplitude and 2 ms duration. Here, myoplasmic $Ca^{2+}$ ($[Ca^{2+}]_i$), which couples the electrical and $Ca^{2+}$ subsystems, is clamped and treated as a parameter. This variant of the model is 7-dimensional and bears strong resemblance to the Luo-Rudy I model

variant analyzed in [22]; in that work the rapid AP-initiating transient $I_{\mathrm{Na}}$ dynamics were removed, here they are retained.

The $Ca^{2+}$-clamped model behaviors are then compared to those of the full model. However, the variant of the full model investigated here excludes the spontaneous $Ca^{2+}$ release mechanism included in [31]. This full model variant is the same as (2.1) with the addition of 3 dynamic variables that represent $Ca^{2+}$ concentrations in the myoplasm and in each of two sub-compartments of the SR. This full model is 10-dimensional (see Appendix A).

The full dynamic $Ca^{2+}$ model variant presents analytical challenges in that its $Ca^{2+}$ dynamics are formulated with an explicit dependence on time; it is non-autonomous. However, dimensional and empirical analysis reveal that the meaningful $Ca^{2+}$ dynamics, as they effect the emergence and properties of EADs, can be recapitulated using a reduced autonomous model. Hence, to understand the dynamics of $Ca^{2+}$-induced EADs we analyze a surrogate autonomous dynamic $Ca^{2+}$ model where the dynamic variables representing the SR subcompartment $Ca^{2+}$ concentrations are removed. This reduced dynamic $Ca^{2+}$ model is 8-dimensional.

Specific parameters are varied to examine and analyze response behaviors of each model where specified. Otherwise, all parameter values are identical to those specified in [31] (see Appendix A). When varied, these parameter values are given in the corresponding figures or main text. Under all parameter variations considered, except where explicitly stated otherwise, each model (absent $I_{\mathrm{stim}}$) possesses 3 equilibria: a stable equilibrium, $E_1$, and two additional unstable equilibria, $E_2$ and $E_3$. Equilibrium $E_1$ sets the resting membrane potential of the cell while equilibria $E_2$ and $E_3$ have depolarized membrane potentials. Equilibrium $E_2$ is a saddle spiral and $E_3$ is a saddle point. The model code and computer programs used to generate the results are available at: www.math.fsu.edu/∼bertram/software/cardiac.

**2.1. Luo-Rudy II produces EADs without $Ca^{2+}$ dynamics.** We begin by analyzing the LRII model cell under clamped-$Ca^{2+}$ conditions. That is, we fix the value of the $[Ca^{2+}]_{\mathrm{i}}$ variable and treat it as a parameter of the purely electrical subsystem. In this way, we focus on EADs that are purely electrical in nature. This treatment separates the two components of the model in a way that is difficult to do experimentally.

One of the prevailing biophysical explanations for the generation of EADs is that they occur when inward currents dominate outward currents in magnitude and/or duration during the plateau phase of an AP [42,43]. The basis for this explanation lies in the EAD-producing effects of many pharmacological interventions which are known to either enhance inward $Ca^{2+}$ or $Na^{+}$currents or suppress outward $K^{+}$currents. One such EAD-producing chemical element, $Cs^{+}$, has been shown to block both $I_{\mathrm{K}}$ and $I_{\mathrm{K1}}$ at high concentrations [12, 36]. In this section, we simulate the application of $Cs^{+}$to test whether this leads to EADs in the clamped-$Ca^{2+}$ model cell.

We simulate the application of $Cs^{+}$by constructing a uniform grid in the two parameter ($\alpha_{I_{\mathrm{K}},I_{\mathrm{K1}}}$, $[Ca^{2+}]_{\mathrm{i}}$) plane (Fig. 3) on which to test model responses. The parameter $\alpha_{I_{\mathrm{K}},I_{\mathrm{K1}}}$is a multiplicative weight that scales both $I_{\mathrm{K}}$ and $I_{\mathrm{K1}}$ uniformly; the value $\alpha_{I_{\mathrm{K}},I_{\mathrm{K1}}}$=1 corresponds to the default setting while $\alpha_{I_{\mathrm{K}},I_{\mathrm{K1}}}$<1 corresponds to decrements in the maximal conductances of $I_{\mathrm{K}}$ and $I_{\mathrm{K1}}$. Clamped $[Ca^{2+}]_{\mathrm{i}}$ is varied from 0.12 $\mu$M to 1 $\mu$M. The lower bound, 0.12 $\mu$M, is the resting level of $[Ca^{2+}]_{\mathrm{i}}$ from the full model under the default parameter set (see Appendix A). The upper bound, 1 $\mu$M, is approximately the maximum value of the $[Ca^{2+}]_{\mathrm{i}}$ transient during a standard model AP. To determine behavior, at each point in the 300 × 300 parameter grid the

model was integrated for 10,000 ms using equilibrium $E_1$ as initial condition. When $E_1$ is stable, it sets the resting membrane potential. To initiate an AP at each grid point, a current pulse of amplitude 30 $\mu$A/cm$^2$ and 2 ms duration was applied.

Figure 3a shows the results of these simulations in terms of the type of behavior elicited. The light green region ('No EADs') denotes parameter sets that produce standard APs without EADs. The white region ('RF') denotes the set of parameters that leads to repolarization failure, where the cell remains depolarized at an elevated membrane potential following the pulse. The light pink region ('Auto') in the top left corner of the panel denotes parameter sets that elicit what is referred to as "automaticity" in cardiac literature—called "tonic spiking" in neuroscience—in the absence of a current pulse. Finally, the red striped region ('EADs') denotes parameter sets that produce AP-prolonging EADs.

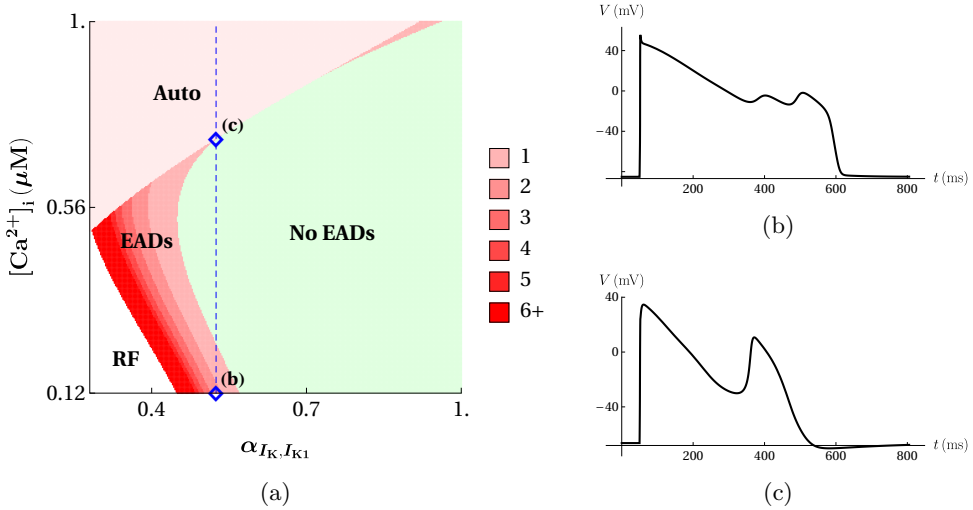


Fig. 3: **Two-parameter diagram of the clamped-$Ca^{2+}$model responses to $Cs^+$ administration and varied $[Ca^{2+}]_i$ contains phase-2 and phase-3 EADs.** (a) Simulated responses to a single pulse reveal four regions of behavior: No EADs (light green), EADs (red), RF (repolarization failure, white), and Auto (automaticity, solid pink). Within the EADs region, the number of EADs elicited is distinguished by different shades of red (see legend). A superimposed dashed (blue) vertical segment at $\alpha_{I_K,I_{K1}}$=0.5248 marks a slice along which EADs are produced at either low or high $[Ca^{2+}]_i$ (blue diamond markers '(b)' and '(c)', resp.). (b) Voltage trace of the '(b)' marker from (a) shows two phase-2 EADs; $[Ca^{2+}]_i$=0.12 $\mu$M. (c) Voltage trace of the '(c)' marker from (a) shows one phase-3 EAD; $[Ca^{2+}]_i$=0.7213 $\mu$M.

The red hue in the EAD region represents the number of EADs evoked with that parameter combination. Darker shades indicate more EADs. Within the darkest shaded strip, for instance, 6 or more EADs are evoked in the AP that results from a single current pulse; some points in this strip near the repolarization failure boundary produce as many as 80+ EADs. Hence, for the lower values of the clamped $[Ca^{2+}]_i$, as $\alpha_{I_K,I_{K1}}$ is decreased, the response to a current stimulus transitions from a standard AP, to an AP with EADs, and finally to repolarization failure at the lowest $\alpha_{I_K,I_{K1}}$

values. In addition, within the 'EADs region', the area of a subregion corresponding to more EADs is smaller than that corresponding to fewer EADs. Thus, if a point is selected in the EADs region at random, then APs exhibiting few EADs are more probable than APs exhibiting many EADs.

The Auto region in Fig. 3a corresponds to parameter values in which the rest state, $E_1$, has undergone a Hopf bifurcation and is unstable. The only attractor of the system is a stable limit cycle, so APs are produced periodically. The loss of stability of $E_1$ is unrelated to the mechanism for EAD generation, so the transition from normal APs to repolarization failure may or may not have an intervening interval of EADs. That is, for some values of $[Ca^{2+}]_i$ the transition is abrupt, switching from normal APs to spontaneous periodic AP production as $\alpha_{I_K,I_{K1}}$ is decreased, while with other values of $[Ca^{2+}]_i$ there is an intervening interval of EADs.

**The clamped-$Ca^{2+}$ model produces phase-2 and phase-3 EADs.** One key observation from Fig. 3a is that the relationship between (fixed) $[Ca^{2+}]_i$ and EAD production is non-monotonic. This is illustrated by following the dashed vertical blue line segment superimposed on the grid at $\alpha_{I_K,I_{K1}} = 0.5248$. EADs are produced at both lower (diamond labeled '**(b)**') and higher (diamond labeled '**(c)**') values of $[Ca^{2+}]_i$, but not at intermediate values. However, the timing of the EADs is very different at the low and high $[Ca^{2+}]_i$ values. The EADs of Fig. 3b occur during the plateau phase, or phase 2, of the AP, and have been termed *phase-2 EADs*. In contrast, the EADs of Fig. 3c occur during the repolarization (i.e., falling) phase, or phase 3, of the AP after an abbreviated phase 2; this class of EADs is initiated at lower take-off potentials and has been termed *phase-3 EADs*. This distinction is important because it shows that $Ca^{2+}$ dynamics are not needed for either of these two classes of EADs, but the $Ca^{2+}$ level may be a determining factor in which type is generated.

Though the partitioning of EAD production into those obtained at low $[Ca^{2+}]_i$ and those obtained at high $[Ca^{2+}]_i$ is convenient, it does not capture the cases in which EADs are produced for a wide range of intermediate $[Ca^{2+}]_i$ levels (see Fig. 3a). A more useful approach is to understand the *dynamics underlying the EADs*, rather than taking a biophysical approach that focuses on the contributions of different ionic mechanisms. We use this approach next, taking advantage of the timescale separation between different sets of variables.

## 3. Fast-slow analysis reveals a mechanism for EAD generation.

In this section, we use fast-slow analysis [3,18] to uncover the EAD-generating mechanisms for both of these EAD types produced when $Ca^{2+}$ is clamped. Fast-slow analysis leverages the multi-timescale structure of a model system to split it into lower-dimensional, more analytically tractable, subsystems. Each subsystem is analyzed semi-independently and the results stitched together to explain and predict system behavior.

### 3.1. The Luo-Rudy II Model is a Multi-Timescale System.

Dimensional analysis of (2.1) reveals that the clamped-$Ca^{2+}$ Luo-Rudy II model has a multiple timescale structure. The voltage, $V$, and gating variables $m$ ($I_{Na}$ activation) and $h$ (fast $I_{Na}$ inactivation) are superfast with timescales that are $\mathcal{O}(10^{-1})$ ms. The gating variables $j$ (slow $I_{Na}$ inactivation), and $d$ ($I_{Ca\text{-}L}$ activation) are fast with timescales that are $\mathcal{O}(10^0)$ ms. The variable $f$ ($I_{Ca\text{-}L}$ inactivation) is slow with timescale $\mathcal{O}(10^1)$ ms. The variable $x$ ($I_K$ activation) is superslow with timescale $\mathcal{O}(10^2)$ ms. Hence, the biophysical clamped-$Ca^{2+}$ model (2.1) can be recast as a singular perturbation problem containing multiple timescales.

With more than two timescales identified, the question of how to leverage this structure to explain EADs arises. In previous work analyzing EADs in the similarly structured Luo-Rudy I model, we found that a two-timescale splitting was sufficient for illuminating the dynamical drivers of myriad EAD behaviors [22]. We also found that treating both $f$ and $x$ (identically named in that and this model) as comprising the slow subsystem provided explanatory and predictive advantages over the more traditional 1-slow approach. In what follows, we show that a two-timescale splitting of (2.1) with slow variables $(f, x)$ and fast variables $(V, m, h, j, d)$ provides a comprehensive picture of the dynamical drivers underlying EAD behavior. The timescale separation is increased when the membrane capacitance, $C_m$, is reduced, and we refer to the $C_m \to 0$ limit as the *singular limit*. The figures and text that follow are presented in terms of the original model variables.

**3.2. The Fast Subsystem Lacks a Mechanism for EAD Generation.** We first analyze the equilibria and bifurcation structure of the fast subsystem, treating the slow variables $f$ and $x$ as bifurcation parameters. The equilibria of the fast subsystem form a 2D surface, called the *critical manifold*, within the 7D phase space. The critical manifold can be expressed globally as a graph over the coordinates $(V, x)$:

$$\begin{aligned} f &= \frac{-\sum I_{\text{ion}} + I_{\text{Ca-L}}}{d_\infty(V)\, f_{\text{Ca}}([\text{Ca}^{2+}]_{\text{i}})\,(\bar{I}_{\text{Ca}} + \bar{I}_{\text{Ca,Na}} + \bar{I}_{\text{Ca,K}})} =: f_S(V, x) \\ m &= m_\infty(V) \\ h &= h_\infty(V) \\ j &= j_\infty(V) \\ d &= d_\infty(V). \end{aligned} \tag{3.1}$$

Figure 4 shows the resulting critical manifold for each parameter set used in Figs. 3b and 3c projected into $(f, x, V)$ phase space. In both cases the critical manifold is cubic-shaped with upper and lower attracting sheets, $S_0^{a,+}$ and $S_0^{a,-}$ (blue surfaces), and a middle sheet, $S_0^s$ (red surface), of saddle-type equilibria. The upper stable sheet, $S_0^{a,+}$, meets the unstable sheet, $S_0^s$ at a 1D curve, $L$ (green), of saddle-node, or fold, bifurcations. The lower attracting and saddle sheets also meet at a fold curve, but this occurs far outside the physiologically relevant domain and is not shown. These 1D curves mark the only bifurcations that the fast subsystem undergoes through meaningful variation (as parameters) in $f$ and $x$. That is, the fast subsystem does not possess Hopf bifurcations, which have been suggested elsewhere as the dynamical mechanism underlying the generation of EADs [25, 27, 42, 51].

With this equilibrium and bifurcation structure, solutions of the fast subsystem that are initialized away from the critical manifold will converge to the appropriate attracting sheet in "fast" time. Once solutions of the fast subsystem get sufficiently close to an attracting sheet of the critical manifold, the dynamics switch to those described by the slow subsystem and evolve in "slow" time.

**3.3. The Slow Subsystem Possesses a Folded Node Singularity.** Within the slow subsystem, the fast variables $V, m, h, j$ and $d$ are slaved to the critical manifold, adjusting instantaneously to the slow motions of $f$ and $x$. The critical manifold then is the interface between the fast and slow subsystems: the fast subsystem produces rapid contraction to the appropriate attracting sheet, where the slow subsystem takes over and guides solutions along this sheet. The dynamics can switch from slow back to fast at the regular fold points of the critical manifold.

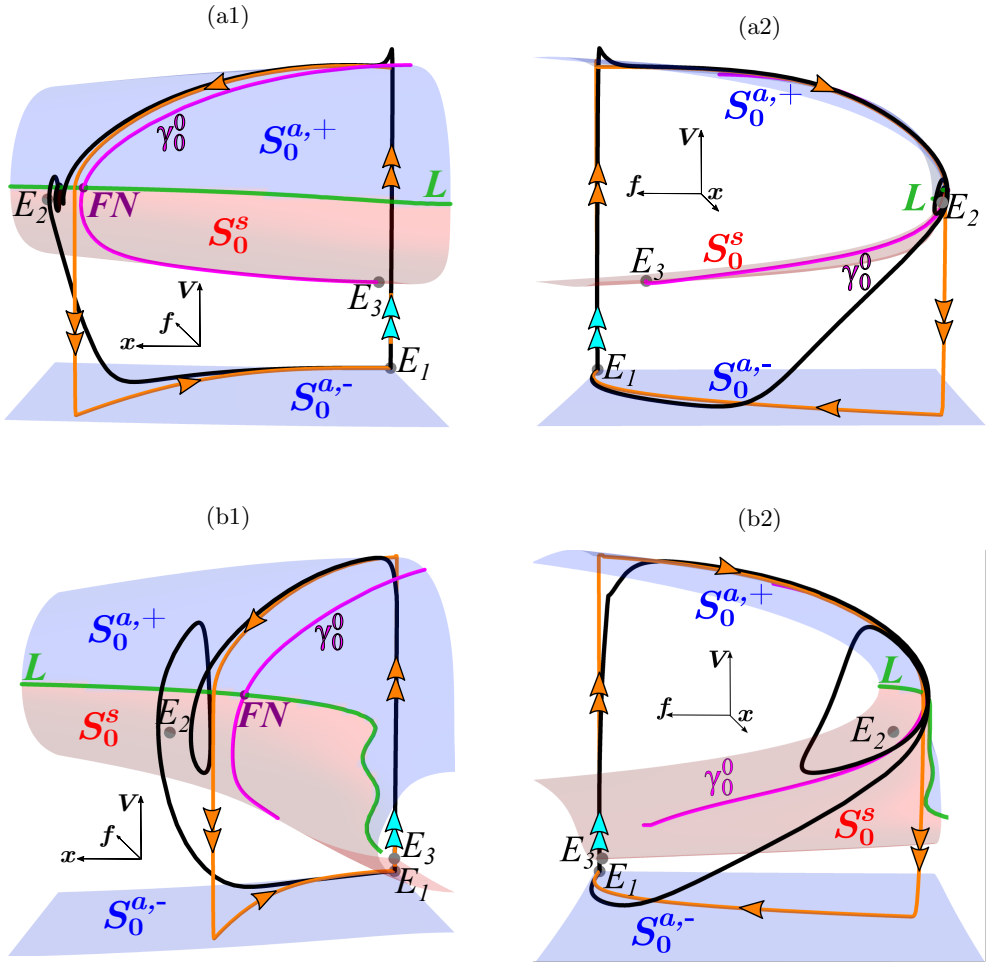


Fig. 4: **Two views of the critical manifold, the fast-slow solution approximation, and the full solution trajectory projected into $(f, x, V)$ space for each trace in Figs. 3b and 3c.** Each row shows two views of the same projection. In all panels the critical manifold is comprised of attracting ($S_0^{a,\pm}$, blue) and saddle-type ($S_0^s$, red) sheets which meet at 1D fold curves. Only the upper fold ($L$, green) is shown. Superimposed on each critical manifold is the true solution (black) and its fast-slow analog (orange). Each fast-slow solution is composed of an initial fast segment triggered by $I_{\text{stim}}$ (double cyan arrows), an ensuing rapid upstroke (double orange arrows) to $S_0^{a,+}$, a subsequent slow segment along $S_0^{a,+}$ (single orange arrow) toward $L$, a consequent rapid expulsion from $L$ toward $S_0^{a,-}$ (double orange arrows), and a slow return (single orange arrow) to stable equilibrium, $E_1$ (equilibria $E_2$ and $E_3$ are unstable). Within $L$ there is a folded node singularity (FN, purple marker) of the desingularized slow subsystem and $\gamma_0^0$ (magenta) is its associated singular strong canard (see main text). (a1) $(x, V)$-dominant view corresponding to Fig. 3b. (a2) $(f, V)$-dominant view corresponding to Fig. 3b. (b1) $(x, V)$-dominant view corresponding to Fig. 3c. (b2) $(f, V)$-dominant view corresponding to Fig. 3c.

For both parameter sets shown in Fig. 4 we find, using the procedure outlined in [55], that the slow subsystem possesses two types of singularities: true singularities (equilibria) and *folded* singularities [48]. The positions of the true singularities, $E_1$ (stable node), $E_2$ (saddle point), and $E_3$ (saddle point) in phase space remain unchanged under variation in $C_m$. The single folded singularity (Fig. 4, FN, purple marker), which lies along the fold, $L$, is of node type; classification of folded singularities is determined through linearization of the associated desingularized reduced problem. Associated with the folded node are a pair of distinguished slow subsystem solutions that correspond to its strong and weak eigendirections. They are respectively called the *singular strong canard* (Fig. 4 $\gamma_0^0$, magenta) and the *singular weak canard* (not pictured).

The region of $S_0^{a,+}$ bounded above by the singular strong canard, $\gamma_0^0$, and below by the fold curve, $L$, is called the *singular funnel*. Within $S_0^{a,+}$, the singular funnel is the basin of attraction for the folded node. Solutions of the slow subsystem initialized in the singular funnel evolve toward the folded node, where they cross from $S_0^{a,+}$ to $S_0^s$ with finite speed, and follow $S_0^s$ for $\mathcal{O}(1)$ times on the slow timescale. These *singular canards* and their non-singular counterparts give rise to small amplitude oscillations in the vicinity of the folded node [48,54]. In ours and others' works, it has been shown that EADs are organized by a folded node of the slow subsystem [22,26,53].

**3.4. Singular solution segments along $S_0^{a,+}$ predict no EADs.** The fast and slow subsystems are used to construct singular approximations of the EAD-containing solutions shown in Figs. 3b, 3c. This is done by concatenating alternating fast and slow solution segments. In contrast to some other models in which fast-slow techniques have been applied [25,26,45,53], the generation of APs here is not spontaneous and requires a sufficiently large stimulus, $I_{\text{stim}}$.

Superimposed on both critical manifolds shown in Figure 4 (rows are different views of the same projection) is the resulting singular approximation (orange), alongside its associated full solution (black), in response to an $I_{\text{stim}}$ pulse. Under the singular limit, a sufficiently strong stimulus (denoted by double cyan arrows) injects the solution into the basin of attraction of $S_0^{a,+}$. The ensuing solution segment, governed by the fast subsystem, rapidly converges to $S_0^{a,+}$ (double orange arrows upward). Once on $S_0^{a,+}$, outside the singular funnel, the slow subsystem guides the slow segment (single orange arrow) along the critical manifold toward the fold curve, $L$. Once $L$ is reached, the fast subsystem takes over and the orbit transitions rapidly (double orange arrows downward) to the lower attracting sheet, $S_0^{a,-}$. On $S_0^{a,-}$, the slow subsystem takes over again and returns the solution (single orange arrow) to rest, $E_1$, completing the construction.

Comparing the singular to the full solution in each of Figs. 4 a1 and b1, we find that the two are nearly aligned from the initial $I_{\text{stim}}$ pulse until the solutions get within the vicinity of the fold, $L$. Both the singular and non-singular solutions lie on the left-hand side of $\gamma_0^0$, near but just outside of the singular funnel. That is, the singular solution trajectory in each case is not funneled through the folded node (FN, purple markers) but instead, exhibits relaxation-type fast switching at $L$. Hence, the singular solutions do not predict the occurrence of canard-induced EAD oscillations in the full solution. In light of this, we investigate how the critical manifold and its singular funnel perturb for $0 < C_m \leq 1$ to determine whether the EADs observed are in fact canard-induced.

**4. EADs are generated by evolution along twisted slow manifolds.** Although the singular solution approximations do not predict EADs in the full system,

the folded critical manifold and the folded node revealed by our fast-slow analysis still leaves open the possibility that canards present away from the singular limit are responsible for the EADs. To show that this is indeed the case, we investigate how the sheets of the critical manifold smoothly perturb to *locally invariant slow manifolds* for $C_m(\propto \epsilon) > 0$ (small). We further compute continuations of these slow manifolds for $C_m \to 1$ and find that the local twisting is key to understanding the genesis and properties of EADs.

**4.1. The twisted region of the slow manifold perturbs toward the EAD oscillations of full system solutions.** Fenichel theory [9, 18] guarantees that the sections of the critical manifold bounded away from the fold curve, $L$, perturb smoothly to nearby locally invariant slow manifolds of the perturbed flow. Further, the local attraction/repulsion properties of these sets also persist. However, the EAD oscillations occur in the vicinity of $L$—where traditional Fenichel theory does not apply. Canard theory [24, 54] extends the Fenichel results into the neighborhood of the fold, and the folded node in particular.

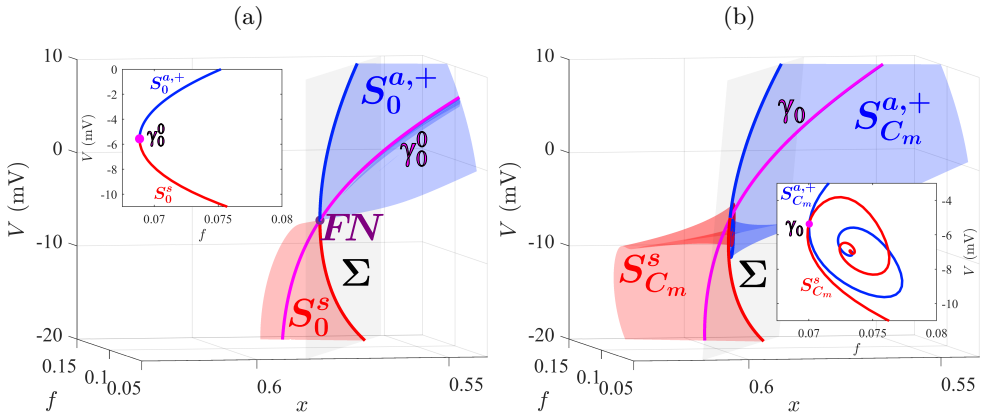


Fig. 5: **Sheets of the critical manifold, $S_0^{a,+}$ and $S_0^s$, perturb to twisted slow manifolds, $S_{C_m}^{a,+}$ and $S_{C_m}^s$, in the vicinity of the folded node, $FN$.** (a) Sheets $S_0^{a,+}$ (blue) and $S_0^s$ (red) are computed up to the hyperplane $\Sigma$ (gray) containing $FN$ (purple marker) with the singular strong canard, $\gamma_0^0$ (magenta), superimposed. Inset is the projection of the intersections of $S_0^{a,+}$, $S_0^s$, and $\gamma_0^0$ with $\Sigma$ into $(f, V)$ phase space. (b) Perturbed sheets $S_{C_m}^{a,+}$ (blue) and $S_{C_m}^s$ (red), computed up to the hyperplane $\Sigma$, become twisted in the vicinity of $FN$ (see inset) and the strong maximal canard, $\gamma_0$ (magenta), shifts toward larger $x$-coordinate values in phase space. Inset is the projection of the intersections of $S_{C_m}^{a,+}$, $S_{C_m}^s$, and $\gamma_0$ with $\Sigma$ into $(f, V)$ phase space. Note the emergent spiraling.

Canard theory holds that in the vicinity of the folded node, for $C_m > 0$ small, $S_0^{a,+}$ and $S_0^s$ perturb smoothly to slow manifolds $S_{C_m}^{a,+}$ and $S_{C_m}^s$, respectively (see Fig. 5), which twist around the (perturbed) weak canard [7, 48, 54]. In cardiac models with one fast and two slow variables—the canonical splitting under which canard-induced oscillations arise—this local twisting in the vicinity of the folded node induces a finite number of transverse intersections of the attracting and repelling slow manifolds [2,

26,53]. The solution curves along which the two-dimensional slow manifolds intersect in this context are called *maximal canards*. However, in our system, with two slow and five fast variables, maximal canard solutions are no longer transverse intersections of $S^s_{C_m}$ and $S^{a,+}_{C_m}$. To facilitate the analysis and computation of canards in such a case, center manifold theory has been used to justify reducing a ($m$,2)–fast-slow problem near a fold, with $m \geq 1$ but finite, to a (1,2)–fast-slow problem [5, 44]. However, we follow [13] and define and compute canards as solutions of the full system (2.1) which transition from the stable manifold $S^{a,+}_{C_m}$ to the unstable saddle manifold $S^s_{C_m}$ and follow $S^s_{C_m}$ for long $\mathcal{O}(1)$ times on the slow timescale. That is, we show that the homotopic continuation methods developed in [13] can be extended to numerically compute the canards and slow manifolds of the full 7D model (see Appendix C).

Figure 5 represents the manner in which the sheets of the critical manifold, $S^{a,+}_0$ (blue) and $S^s_0$ (red), from Figs. 4a1 and 4a2 persist as slow manifolds, $S^{a,+}_{C_m}$ (blue) and $S^s_{C_m}$ (red), as $C_m$ is increased from 0 (Fig. 5a) to 0.5 $\mu$F/cm$^2$ (Fig. 5b). In both cases, the corresponding strong canard ($\gamma^0_0$ for $C_m = 0$ and $\gamma_0$ for $C_m = 0.5$) is superimposed on the critical/slow manifold(s) and the region of the phase space in view is fixed. The local structure of the slow manifold unfolding shown in Fig. 5 is used to represent what occurs in the vicinity of the folded node for both parameter sets pictured in Fig. 4.

For computation and visualization purposes, all slow manifolds are computed up to the codimension-1 hyperplane $\Sigma$ (see Appendix C). Whereas the standard set-up chooses $\Sigma$ such that it contains the folded singularity, the significant movement of the twisted funnel in phase space as we both increase $C_m$ away from the singular limit and as we vary system parameters requires a more general set-up. We instead choose $\Sigma$ to contain the turning point of the strong canard, $\gamma_0$, and let the orientation of $\Sigma$ vary with parameters. Each inset shows the intersection curves $S^{a,+} \cap \Sigma$ (blue) and $S^s \cap \Sigma$ (red) along with the intersection point $\gamma_0 \cap \Sigma$ (magenta) projected to the $(f, V)$-plane. Although Fig. 5b appears to convey that $S^{a,+}_{C_m}$ (blue) and $S^s_{C_m}$ (red) intersect one another, this is simply an artifact of projecting the 7D dynamics into a lower-dimensional subspace.

For the parameter set shown in Fig. 5, tracking the movement of the funnel region reveals that as $C_m$ is increased from 0, the funnel moves in phase space towards the EAD oscillations observed at $C_m = 1$ $\mu$F/cm$^2$. For instance, the $x$-coordinate of the turning point of the strong canard increases from $x_p = 0.5804$ at $C_m = 0$ $\mu$F/cm$^2$ to $x_p = 0.6016$ at $C_m = 0.5$ $\mu$F/cm$^2$. Hence, we must fully unfold the slow manifolds to $C_m = 1$ $\mu$F/cm$^2$ to determine whether the twisted funnel structure underlies EAD generation.

**4.2. Both clamped-$Ca^{2+}$ EAD behaviors are canard-induced.** Here, we fully unfold the slow manifolds present for both parameter sets shown in Fig. 4 to determine whether the observed EAD behaviors are canard-induced. To do so, we must examine the finer structure of the slow manifolds elaborated by canard theory. According to canard theory, the maximal canards ($\gamma_0$, $\gamma_1$, $\gamma_2$,..., $\gamma_n$) that result from the local twisting of the slow manifolds partition the funnel region of $S^{a,+}_{C_m}$ into rotational sectors, or strips. Each rotational sector prescribes a particular number of small amplitude oscillations to be produced in entrant solutions. Solutions injected into the trivial rotational sector outside the funnel region (bounded by $\gamma_0$) do not exhibit small amplitude oscillations, while solutions injected into the rotational sector between the maximal canards $\gamma_{i-1}$ and $\gamma_i$ for $i = 1, 2, ..., n$ exhibit $i$ small oscillations before exiting the funnel (by rapidly transitioning to either $S^{a,+}_{C_m}$ or $S^{a,-}_{C_m}$).

This canard structure, embedded within the twisted slow manifolds, constrains the behavior of entrant solutions. Hence, it can be used to predict whether and how many small oscillations, or EADs, will be produced under a given set of model conditions. This provides a means of testing whether canards are the dynamical mechanism underlying EAD generation and properties.

Figure 6 shows closeup views of the continuations of the twisted slow manifold regions of $(f, x, V)$ phase space for both low $[Ca^{2+}]_i$ phase-2 EADs (Fig. 6a) and high $[Ca^{2+}]_i$ phase-3 EADs (Fig. 6b). In both cases, the solution trajectory ($\Gamma$, black) and the leading maximal canards ($\gamma_0$, magenta; $\gamma_1$, cyan; $\gamma_2$, orange) are superimposed on the continuations of the slow manifolds, $S^{a,+}_{C_m}$ (blue) and $S^s_{C_m}$ (red). Corresponding voltage traces are inset.

Canard theory predicts that solutions that lie in the rotational sector between $\gamma_0$ and $\gamma_1$ should contain one EAD and that solutions that lie in the rotational sector between $\gamma_1$ and $\gamma_2$ should contain two EADs. The black solution segment shown in Figs. 6a lies between maximal canards $\gamma_1$ and $\gamma_2$ and, in accordance with canard theory, exhibits two small oscillations (EADs) before exiting the funnel. Similarly, the black segment in Fig. 6b lies between $\gamma_0$ and $\gamma_1$ (see inset) and exhibits one EAD oscillation, also in agreement with the predictions from canard theory. This affirms that maximal canards demarcate the boundaries in phase space across which the number of EADs produced is incremented/decremented. Accordingly, the EADs observed under both biophysical conditions are canard-induced oscillations.

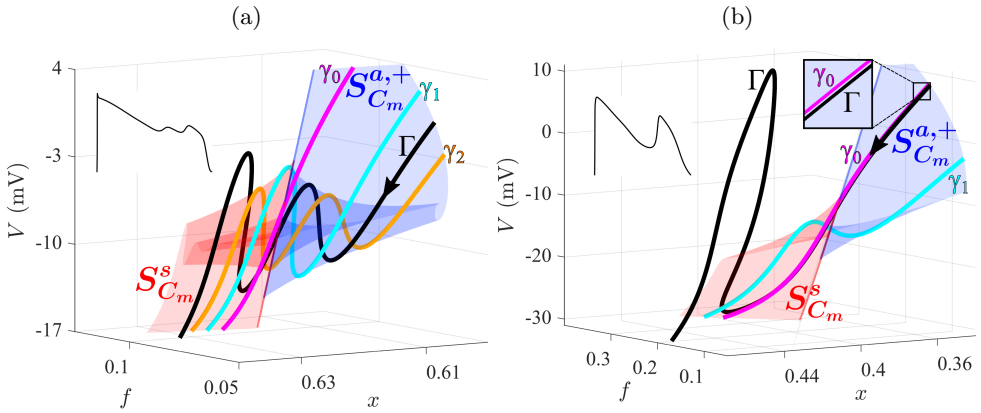


Fig. 6: **Canards underlie low $[Ca^{2+}]_i$ phase-2 EADs and high $[Ca^{2+}]_i$ phase-3 EADs** Both panels are closeup views of the twisted slow manifolds, $S^{a,+}_{C_m}$ (blue) and $S^s_{C_m}$ (red), in the vicinity of EAD-exhibiting solution segments ($\Gamma$, black) in $(f, x, V)$ phase space. Superimposed are maximal canard segments–$\gamma_0$ (magenta), $\gamma_1$ (cyan), and $\gamma_2$ (orange)–which serve as phase space boundaries for the addition/reduction of EAD number. (a) Low $[Ca^{2+}]_i$ phase-2 EADs corresponding to trace Fig. 3b (see inset). (b) High $[Ca^{2+}]_i$ phase-3 EADs corresponding to trace Fig. 3c (see inset).

**4.3. Canards can explain properties of phase-3 EADs.** Viewing EADs from the canard viewpoint provides potential insights into the emergence and properties of phase-3 EADs. In [42], it is argued that the dynamical mechanism underlying

the genesis of phase-3 EADs is the same as the dynamical mechanism underlying phase-2 EADs: a Hopf bifurcation in the fast subsystem. However, this explanation does not account for the most notable differences between phase-2 and phase-3 EADs. First, phase-3 EADs have a significantly lower takeoff potential and larger amplitude than phase-2 EADs [10]. Second, phase-3 EADs are more difficult to elicit in isolated cell and tissue preparation experiments than phase-2 EADs [10, 42]. Neither of these findings would be expected if a Hopf bifurcation in the fast subsystem were responsible for both phase-2 and phase-3 EADS. However, both findings are expected when the EADs are viewed through canard analysis, as we describe next.

In Fig. 6b, which shows the phase-3 EAD in the $(f, x, V)$ phase space, the solution segment, $\Gamma$, lies very close to $\gamma_0$. The closer a solution lies to $\gamma_0$, the longer it can follow $S^s_{C_m}$ before being repelled. Hence, because $\Gamma$ lies close to $\gamma_0$, it reaches a much lower takeoff potential before jumping back to $S^{a,+}_{C_m}$. This results in an EAD that occurs late in the repolarization phase of the AP, and has large amplitude. These are defining properties of a phase-3 EAD. Furthermore, the rarity with which phase-3 EADs are observed in experiments can also be explained as a consequence of the required proximity between $\Gamma$ and $\gamma_0$: it is rare for a solution trajectory to be injected so close to a maximal canard.

**5. Canards underlie $Ca^{2+}$ dynamics-mediated EADs.** Our analysis has demonstrated that the $Ca^{2+}$ level can play an important and complex role in the generation of different classes of EADs even when $[Ca^{2+}]_i$ remains fixed. In doing so, we have shown that $Ca^{2+}$ dynamics are not essential to EAD production; EADs can occur even when $[Ca^{2+}]_i$ is clamped. Here, we introduce the $Ca^{2+}$ dynamics (see (A.1b)) into our analysis to investigate behaviors that cannot be reproduced when the $Ca^{2+}$ concentration is clamped. For this analysis, the cell is subject to periodic pacing, with a stimulus period of 2000 ms, until the pulsed solution converges to a periodic attractor. Unless otherwise noted, all of the time courses in the following analysis are a single period of this attractor AP.

**5.1. The clamped-$Ca^{2+}$ model does not reproduce EADs induced by $Ca^{2+}$ overload.** In [32], the developers of the LRII model investigated its ability to reproduce experimental observations regarding early afterdepolarizations as well as other pathologies across species. In one set of numerical experiments, they showed that under the combined effects of $Na^+$ ion accumulation, increases in the activity of $I_{\text{Ca-L}}$, and ensuing $Ca^{2+}$ overload the model produces robust and repeated EADs over consecutive APs (see Fig. 11 of [32]). These EADs occurred during episodes of spontaneous AP activity as well as during periodic pacing [32]. That is, under these conditions, the full model (see Appendix A) possesses an EAD generating mechanism that is separable from the process of spontaneous $Ca^{2+}$ release from the sarcoplasmic reticulum (SR), yet may still rely on $Ca^{2+}$ dynamics. It is this EAD generating mechanism, which arises in the presence of pathological $Ca^{2+}$ dynamics, that we investigate here.

We first examine whether the EADs produced by the model with $Ca^{2+}$ dynamics (which we refer to as the "dynamic-$Ca^{2+}$ model") can be reproduced by the model with $Ca^{2+}$ clamped (which we refer to as the "clamped-$Ca^{2+}$ model"). In both model contexts, key parameters are set to simulate $Ca^{2+}$ overload ($[Na^+]_i$ = 15 mmol/L, $[Ca^{2+}]_o$ = 3 mmol/L, and $P_{Ca}$ (max $I_{\text{Ca-L}}$ amplitude) = 1.3×0.00054 cm/s). Under these conditions, the AP generated by the dynamic-$Ca^{2+}$ model has a long plateau and two EADs (black curve in Fig. 7a) and a $[Ca^{2+}]_i$ profile consisting of a rapid peak with a slow decline during the AP (black curve in Fig. 7b). In our attempt to

replicate this voltage timecourse with the clamped-$Ca^{2+}$ model, four different values of $[Ca^{2+}]_i$ were used (colored horizontal lines in Fig. 7b). For the lower values of $[Ca^{2+}]_i$, the clamped-$Ca^{2+}$ model produced APs without EADs (blue and magenta traces in Fig. 7a), while for the higher values of $[Ca^{2+}]_i$ it exhibited automaticity (purple and red traces in Fig. 7a). In no case did the clamped-$Ca^{2+}$ model produce a long AP with EADs, in contrast to the dynamic-$Ca^{2+}$ model which generically produces a long AP with EADs in these conditions. Hence, the LRII model reproduces experimental findings that show that some classes of EADs can be abolished through the use of $Ca^{2+}$ chelators and CICR antagonists which essentially clamp the $Ca^{2+}$ concentration.

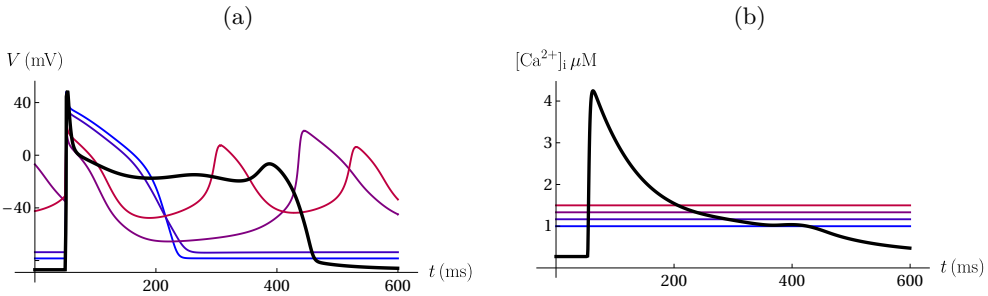


Fig. 7: **$Ca^{2+}$ dynamics are essential for $Ca^{2+}$ overload-induced EADs.** (a) Voltage traces produced by the dynamic-$Ca^{2+}$ model (black) and the clamped-$Ca^{2+}$ model (colored). In each case, parameters were set to replicate the conditions of $Ca^{2+}$ overload ($[Na^+]_i$= 15 mmol/L, $[Ca^{2+}]_o$= 3 mmol/L, 30% increase in $I_{Ca\text{-}L}$ activity). An AP with EADs is produced by the dynamic-$Ca^{2+}$ model, but not by the clamped-$Ca^{2+}$ model. (b) $Ca^{2+}$ levels corresponding to the voltage traces in a are color-coded accordingly.

**5.2. Fast-slow analysis of a minimal dynamic-$Ca^{2+}$ model reveals a curve of folded nodes.** Rather than working with the full dynamic-$Ca^{2+}$ model, we found that the essential elements for EAD production could be retained by performing a model reduction in which the variables $[Ca^{2+}]_{nsr}$ and $[Ca^{2+}]_{jsr}$ are fixed. To fix $[Ca^{2+}]_{nsr}$, we use its comparatively large timescale and weak coupling to $[Ca^{2+}]_i$. To fix $[Ca^{2+}]_{jsr}$, we rely on its vanishing coupling to $[Ca^{2+}]_i$ very shortly after the AP upstroke, long before the EADs are generated (for details, see Appendix A). With these changes, the 8-dimensional "minimal dynamic-$Ca^{2+}$ model" (see Appendix (A.2)) is retained.

To perform a fast-slow analysis of the model (A.2), we first determined the characteristic timescale of $[Ca^{2+}]_i$ empirically. The resulting time constant estimate, $\tau_{[Ca^{2+}]_i,decay} \approx 90$ ms, is on the order of the timescales observed for the slow variables $f$ and $x$. Hence, $[Ca^{2+}]_i$ acts as a third slow variable and the dynamic-$Ca^{2+}$ model can be cast as a singularly perturbed (5,3)–fast-slow problem. This third slow variable is what unfolds a set of system behaviors which cannot be seen in the clamped-$Ca^{2+}$ model.

In [55], it was shown that canard theory extends naturally from the case of two slow variables to the more general case of $k$ slow variables, for any $k \geq 2$ and finite. Further, in [11], it was shown that these theoretical advancements could be used to

explain anomalous delays in $Ca^{2+}$ models with three slow variables. Hence, the canard mechanism responsible for the production of EADs in the (5,2)–fast-slow clamped-$Ca^{2+}$ model may persist as the EAD generating mechanism in the (5,3)–fast-slow dynamic-$Ca^{2+}$ model. In light of this, we undertake a fast-slow analysis of the minimal dynamic-$Ca^{2+}$ model in search of the requisite singular structure which can give rise to canard-mediated EAD behavior.

In our analysis of the fast subsystem of (2.1), we found that even under exhaustive variation in $[Ca^{2+}]_i$, it lacked an EAD generating mechanism. Hence, the fast subsystem of the minimal dynamic-$Ca^{2+}$ model does not possess an EAD generating mechanism and we focus our analysis on the slow subsystem which is a 3D approximation of the minimal dynamic-$Ca^{2+}$ model where the fast variables are at quasi-equilibrium.

The critical manifold, to which solutions are constrained, can be expressed globally as a graph over the coordinates $([Ca^{2+}]_i, x, V)$:

$$
\begin{aligned}
f &= \frac{-\sum I_{\text{ion}} + I_{\text{Ca-L}}}{d_\infty(V)\, f_{\text{Ca}}([Ca^{2+}]_i)\,(\bar{I}_{\text{Ca}} + \bar{I}_{\text{Ca,Na}} + \bar{I}_{\text{Ca,K}})} =: f_{S_2}(V, x, [Ca^{2+}]_i) \\
m &= m_\infty(V) \\
h &= h_\infty(V) \\
j &= j_\infty(V) \\
d &= d_\infty(V).
\end{aligned}
\tag{5.1}
$$

Intuitively, the 3D critical manifold (5.1) can be thought of as a one-parameter ($[Ca^{2+}]_i$) family of 2D critical manifolds (3.1). Hence, it is comprised of upper and lower 3D attracting sets and a middle 3D set of saddle-type. Consequently, the set of fold curves along which the upper attracting and middle saddle-type sets meet forms a 2D surface. Figure 8 shows two different views of this 2D fold surface ($L$, green), which is located near plateau membrane potentials in ($[Ca^{2+}]_i$, $x, V$) phase space. Superimposition of the dynamic $Ca^{2+}$ EAD segment ($\Gamma$, black) atop the fold surface reveals that the EADs occur near the fold surface.

Analysis of the (desingularized) slow subsystem further reveals that the fold surface contains a curve of folded singularities (the collection of orange, red, and purple curve segments in Fig. 8). Each folded singularity within the curve possesses a zero eigenvalue whose associated eigenvector is tangent to the curve. Hence, the stability classification of each folded singularity is determined using the two remaining non-zero eigenvalues [55].

We found that the curve of folded singularities contains segments of folded nodes (purple), points which were shown to organize the canard-mediated EAD behavior of the clamped-$Ca^{2+}$ model (2.1). The curve of folded singularities also contains segments of folded foci (orange) and folded saddles (red). It appears that the EAD solution segment, $\Gamma$, interacts with one of the segments of folded nodes before two EADs ensue. We focus our analysis on this segment of folded nodes, and its potential for understanding EAD production in the dynamic-$Ca^{2+}$ model.

As in the case of two slow variables, associated with each folded node along the segment is a pair of special slow subsystem solutions, a strong and a weak singular canard, which are locally tangent to its strong and weak eigenvectors, respectively. Hence, associated with this (and the other) segment of folded node singularities are a pair of 2D families of distinguished slow subsystem solutions: one family of strong singular canards and the other of weak singular canards. The subset of the family of

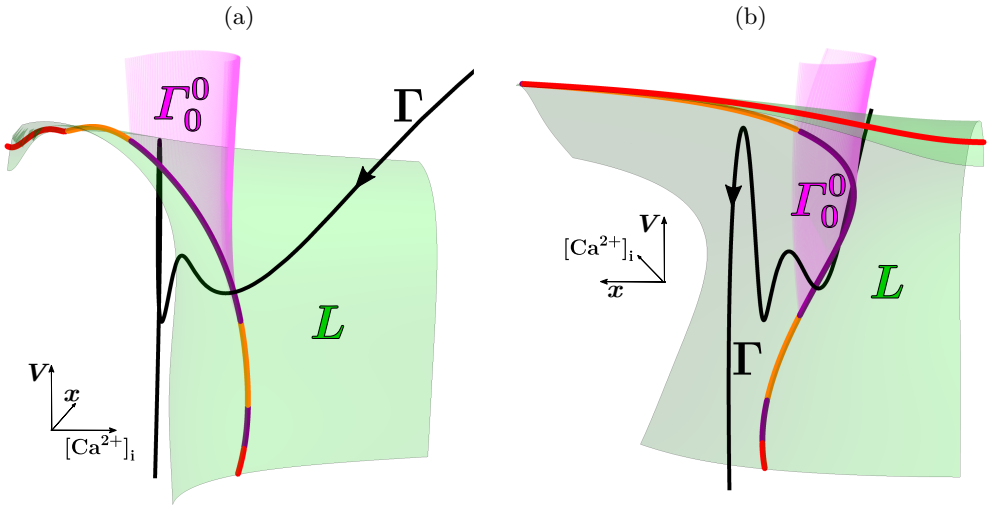


Fig. 8: **Two views of structures involved in EADs generated by the minimal dynamic-$Ca^{2+}$ model.** The fold surface ($L$) is in green. Contained within this surface is a curve of folded singularities containing folded saddles (red), folded foci (orange), and folded nodes (purple). Associated with the folded nodes is a surface of strong singular canards ($\Gamma_0^0$, magenta). Finally, a portion of the system trajectory containing two EADS ($\Gamma$, black) is superimposed.

strong singular canards associated with this segment of folded nodes that lies above the fold surface is pictured in Fig. 8 ($\Gamma_0^0$, magenta).

In contrast with works, such as [11], in which the limiting geometry of the 3D slow subsystem was sufficient to explain fully perturbed solution behavior, our analysis of the clamped-$Ca^{2+}$ model showed that the singular limit can be an unreliable predictor of full solution behavior. Hence, in the next section, we extend existing approaches to the analysis of problems with three slow variables and unfold the limiting geometry of the minimal dynamic-$Ca^{2+}$ slow subsystem to determine whether the EADs are canard-induced.

**5.3. Dynamic-$Ca^{2+}$ EADS are generated by canards.** Fast-slow analysis of (A.2) revealed a folded critical manifold, the existence of sets of folded node singularities, and, in turn, sets of singular canards. We have shown that the perturbed analogs of these structures in the two slow variable problem (2.1) are fundamental in organizing EAD behavior. We use a similar unfolding approach here, increasing the membrane capacitance, $C_m$, away from the singular limit $C_m \to 0$. The aim is to determine whether the resulting maximal canards are responsible for the EADs produced by the dynamic-$Ca^{2+}$ model (A.2).

As is the case with two slow variables, Fenichel theory [9] applies to the portion of the critical manifold that is not near the fold surface. These subsets perturb smoothly to locally invariant 3D slow manifolds whose local attractive/repulsive properties match those of the critical manifold. Furthermore, canard theory applies in the vicinity of the fold surface and, in particular, in the vicinity of the segment of folded

node singularities [55]. That is, the 2D sets of singular strong and weak canards associated with folded node singularities perturb to a finite number of 2D sets of maximal canards. As in the case of two slow variables, these (2D) surfaces of maximal canards partition the (3D) upper attracting and middle saddle-type slow manifolds into (3D) rotational sectors.

The existence of 2D surfaces of maximal canards in the phase space raises questions about how to compute them. We found that the homotopic continuation methods developed in [13] could be extended to accomplish this task. The technical details of the problem set-up and procedure are outlined in Appendix D. Figure 9 shows two illustrative projections of the resulting maximal canard sets and the trajectory containing two EADS (Γ, black) in phase space. Fig. 9a shows the three leading maximal canard surfaces ($\Gamma_0$, magenta; $\Gamma_1$, cyan; $\Gamma_2$, orange) along with a portion of the 2-EAD trajectory, projected into ($x$,$[Ca^{2+}]_i$,$V$) space. Although the true dynamics are in 8D, the trajectory appears to enter the region of phase space between $\Gamma_1$ and $\Gamma_2$, where canard theory would predict that an entrant trajectory should exhibit two small oscillations. Indeed, this is the case; the trajectory exhibits two EADs.

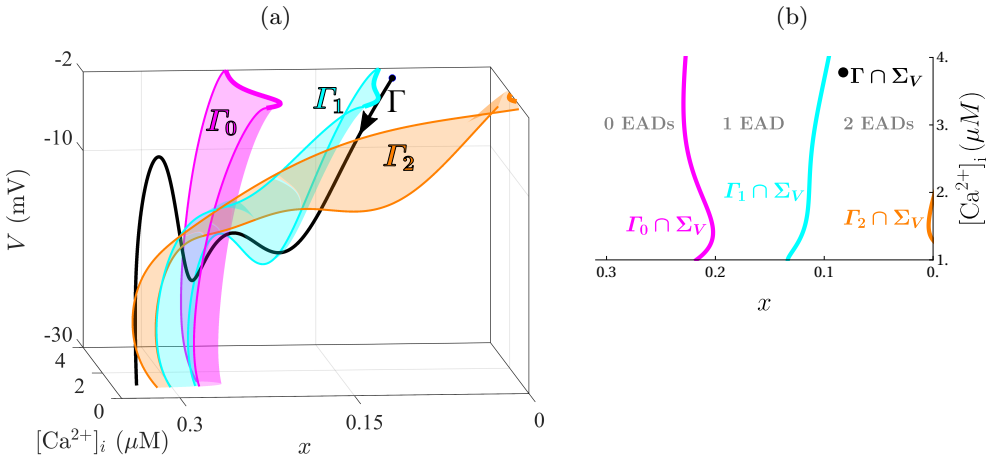


Fig. 9: **Evidence that dynamic-$Ca^{2+}$ EADs are due to canards** (a) 2D sets of maximal canards, $\Gamma_0$ (magenta), $\Gamma_1$ (cyan), and $\Gamma_2$ (orange) are projected into ($[Ca^{2+}]_i$, $x$, $V$) phase space alongside the dynamic-$Ca^{2+}$ EAD solution trajectory (Γ, black). (b) Intersections with the plane $V = -2$ mV ($\Sigma_V$). Both views indicate that the trajectory enters a region of phase space between the maximal canards $\Gamma_1$ and $\Gamma_2$, so that canard theory predicts two small oscillations, in agreement with the two EADS exhibited by Γ.

In Fig. 9b, a 2D view of this arrangement is obtained by projecting the intersections of the maximal canard surfaces and the trajectory with the hyperplane $\Sigma_V = \{(V, m, h, j, d, f, x) \in \mathbb{R}^7 \,|\, V = -2 \text{ mV}\}$ (which lies above the fold surface) onto the ($x$,$[Ca^{2+}]_i$)-plane. Here, the canard surfaces become curves ($\Gamma_0 \cap \Sigma_V$, magenta; $\Gamma_1 \cap \Sigma_V$, cyan; $\Gamma_2 \cap \Sigma_V$, orange) and the trajectory curve is now a point ($\Gamma \cap \Sigma_V$, black). From this, it is again clear that the trajectory enters the region bounded by the maximal canards $\Gamma_1$ and $\Gamma_2$ (labeled as '2 EADs'), so that canard theory predicts

two small oscillations. This match between the canard theory predictions and the number of EADs observed indicates that the EADs are produced by canards.

**5.4. Canard theory explains why reducing $Ca^{2+}$ release from intracellular stores reduces the number of EADs.** It has been shown that manipulations that reduce the release of $Ca^{2+}$ from the SR, such as the use of $Ca^{2+}$ chelators to bind free $Ca^{2+}$ or the use of ryanodine receptor antagonists to block $Ca^{2+}$-induced $Ca^{2+}$ release, also tend to reduce the number of EADs produced or eliminate them altogether [15, 41, 61]. To examine whether this effect could be explained using canard theory, we simulated it by reducing the maximum amplitude of the flux of $Ca^{2+}$ release from the SR, $J_{\text{rel}}$, under $Ca^{2+}$ overload conditions. ($\overline{G}_{\text{rel}} = 20$ reduced to 10 $s^{-1}$ in the full model). In the reduced version of the model, this also requires setting $\overline{[Ca^{2+}]}_{\text{nsr}} \approx 3.5499$ mM. All other parameters remain unchanged.

The effect of this manipulation, in the minimal dynamic-$Ca^{2+}$ model, is to reduce the number of EADs from two to one. This is shown in Fig. 10a, which includes the portion of the trajectory near the EAD, and the three leading maximal canard surfaces. The intersection of each of these objects with $\Sigma_V$ is shown in Fig. 10b. The canard surfaces are only minimally affected by the reduced $Ca^{2+}$ release. There is a greater effect on the trajectory, so that it now enters a different rotational sector. Now the trajectory enters the region between $\Gamma_0$ (magenta) and $\Gamma_1$ (cyan) which, from canard theory, indicates the existence of a single small oscillation. This is again in agreement with the single EAD that is produced by the minimal dynamic-$Ca^{2+}$ model.

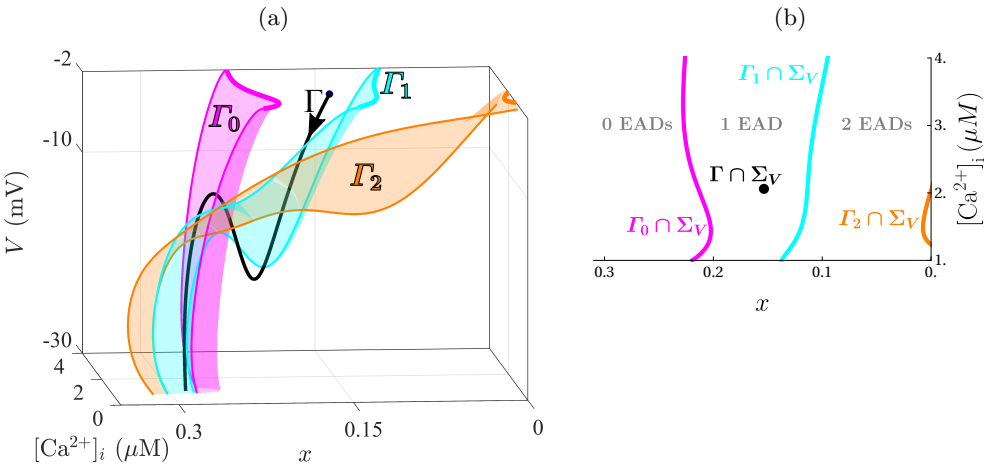


Fig. 10: **Reduction in CICR amplitude decreases EAD number by changing the rotational sector in which the solution, Γ, is injected.** (a) Reduced CICR amplitude has little effect on the maximal canard surfaces, but the trajectory is left-shifted and enters the rotational region between $\Gamma_0$ (magenta) and $\Gamma_1$ (cyan). (b) In the intersection with the plane $V = -2$ mV ($\Sigma_V$), the trajectory lies in the sector in which one small oscillation is predicted by canard theory, in agreement with the single EAD produced by the minimal dynamic-$Ca^{2+}$ model. In this simulation, $\overline{[Ca^{2+}]}_{\text{nsr}}$ is reduced to 3.5499 mM

**5.5. Canards underlie dynamic-$Ca^{2+}$ phase-3 EADs.** We showed that the clamped-$Ca^{2+}$ model produces phase-3 EADs and that it does so as a result of solutions lying close in proximity to maximal canards. It is reasonable then to ask: can the dynamic-$Ca^{2+}$ model produce phase-3 EADs? If so, is proximity to maximal canards still the underlying culprit? Indeed, we find that the dynamic-$Ca^{2+}$ model can produce phase-3 EADs and that they also result from proximity of solutions to maximal canards.

Figure 11 shows a side-by-side comparison of the dynamic-$Ca^{2+}$ phase-2 EADs introduced in Fig. 7 (Fig. 11a) and the phase-3 EAD evoked in response to setting the CICR release flux amplitude parameter, $\overline{G}_{\rm rel} = 21.96235$ 1/s for a single stimulus pulse (Fig. 11b). Although not shown, this value of $\overline{G}_{\rm rel}$ leads to the trajectory being injected into the immediate vicinity of $\Gamma_1$, where the ensuing solution–after an initial phase-2 EAD–follows $\Gamma_1$ to a notably lower take-off potential (≈-31.25 mV in Fig. 11b versus ≈-19.5 mV in Fig. 11a) before jumping back up to $S^{a,+}_{C_m}$. We note that the phase-3 EAD signature shown in Fig. 11b bears striking resemblance to some previous experimental recordings (e.g., compare to Fig. 9c of [35]).

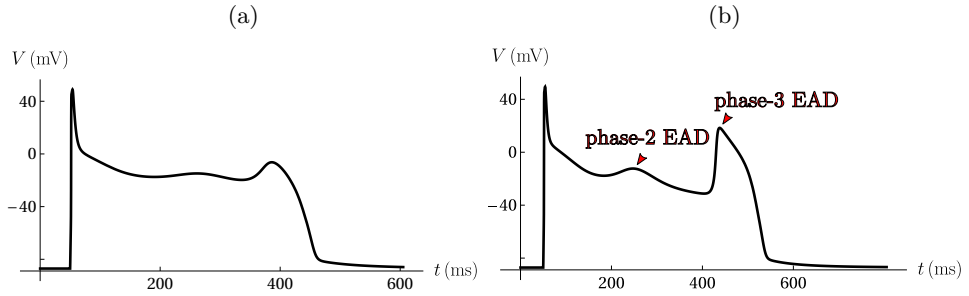


Fig. 11: **. Phase-2 and Phase-3 EADs are produced with the dynamic-$Ca^{2+}$ model.** (a) An AP with two phase-2 EADs generated under $Ca^{2+}$ overload conditions. (b) Proximity of the solution to the 2D maximal canard surface $\Gamma_1$ induces a phase-3 EAD following a phase-2 EAD.

**6. Discussion.** Prior analyses of EADs produced by low-dimensional mathematical models of cardiomyocyte electrical activity have revealed that EADs are canard-induced small oscillations [2, 22, 23, 26, 53]. This canard-based approach to investigating the emergence and properties of EADs provides explanatory and predictive insights that cannot be obtained by other means, but it is most easily applied to models that retain only the essential features of cardiomyocyte electrical activity. Importantly, many of the constituent components of cellular electrical activity which are excluded from these analyses have been shown to play prominent roles in mediating the emergence, properties, and persistence of EADs in cardiomyocytes [4, 31, 35, 41, 46]. Thus, there is a gap between the explanatory and predictive insights provided by canard analysis of low-dimensional models, and the much more limited analysis that comes from computer simulations of higher-dimensional, but more biophysical, models. It is these latter models that are often most helpful in informing experimental and clinical practice.

The current study begins to bridge the gap between the two approaches. It does

so by performing a canard analysis of one of the foundational mathematical models in cardiac electrophysiology, the Luo–Rudy II model [31]. This model includes many biophysical elements that potentially play a role in the generation of EADs, but which have yet to be analyzed using canard-based techniques. Such elements include intracellular $Ca^{2+}$ dynamics and the associated $Ca^{2+}$-dependent transmembrane currents, such as $I_{NaCa}$. We found that even in this more complex model, the EADs produced are most fruitfully cast as canard-induced oscillations. That is, we have demonstrated that the canard-induced EADs identified in the earlier studies of low-dimensional models are still present in a higher-dimensional model. We postulate that EADs generated in the more recent, and more complex, models of cardiomyocyte electrical activity [38, 49, 50] are also due to canards.

One key question in the study of EADs is whether they are mediated by purely electrical factors, i.e., the interaction of ion channels through the membrane potential [16, 17], or whether they also involve the dynamics of intracellular $Ca^{2+}$ following $Ca^{2+}$-induced $Ca^{2+}$ release from the SR [20, 21, 58]. While this mathematical study could not weigh in on this question, it has addressed a related question that is best approached using a mathematical model. In the model, it is possible to clamp the intracellular $Ca^{2+}$ concentration at any level. This is much more difficult to do in experiments, and requires the use of multiple drugs to not only clamp the $Ca^{2+}$, but to set it at the desired concentration. We have taken advantage of this opportunity to address the question of whether, in the Luo-Rudy II model, EADs are generated by purely electrical elements, or whether $Ca^{2+}$ dynamics are also required. We found that, in all cases, the intracellular $Ca^{2+}$ level is important in the determination of whether or not EADs are produced. However, in many cases, the EADs were produced through purely electrical means, with $Ca^{2+}$ serving only as a fixed input to the electrical subsystem. This agrees with experiments in which $Ca^{2+}$ influx was blocked pharmacologically but an electrical $Ca^{2+}$ curent was introduced using the dynamic clamp technique [19, 33, 34] as well as with experiments that showed EADs to persist despite blockade of CICR [35]. However, we also found cases in which EADs are produced only if $Ca^{2+}$ is allowed to vary over the duration of the action potential. That is, in some cases, $Ca^{2+}$ dynamics are an essential ingredient to EAD production. This is consistent with findings that EADs were eliminated when $Ca^{2+}$-induced $Ca^{2+}$ release was blocked pharmacologically [41, 46]. Our results may therefore help to resolve the sometimes conflicting data on EAD production in cardiomyocytes; sometimes $Ca^{2+}$ dynamics are involved in EAD production, and sometimes the EADs are purely electrical in nature (though, even in this case, the $Ca^{2+}$ level affects whether the EADs are triggered). In either case, the EADs produced by the model are brought about by the evolution of solutions along a twisted slow manifold—a twisted slow manifold which is subdivided into regions which dictate EAD number (Fig. 9).

Many of the most well-studied EAD-inducing pharmacological agents exert their effects by blocking $K^+$ channels. Some of these agents are non-selective $K^+$ channel antagonists (e.g., $Cs^+$). We found that the model can produce EADs under simulated administration of these types of agents, even when $[Ca^{2+}]_i$ is clamped (Fig. 3). We showed that non-selectively blocking $K^+$ channels can induce EADs at both (fixed) baseline and elevated $Ca^{2+}$ levels. Surprisingly, the relationship between $[Ca^{2+}]_i$ and EAD production in these cases is non-monotonic. The complexity of the relationship between $[Ca^{2+}]_i$ and EAD production is also demonstrated by the production of both phase-2 and phase-3 EADs (Fig. 3c) at elevated $[Ca^{2+}]_i$ levels.

One advantage of fast-slow analysis of a multi-scale mathematical model is that it allows one to understand dynamical behavior in a deep way that cannot be achieved

through computer simulations alone. For example, we showed that reducing the $Ca^{2+}$ release from intracellular stores had little effect on the canards, but shifted the trajectory in phase space in such a way that it was not influenced by the canards (Fig. 10). Here, EADs were reduced in number, but the mechanism would not be at all apparent from computer simulations alone. Conversely, we demonstrated that both phase-2 and phase-3 EADs can be generated by the same dynamical mechanism, in spite of the fact that the former occurs during the plateau of an action potential, while the latter occurs much later during the repolarizing phase (Fig. 6). These are typically treated as entirely different phenomena in the experimental literature [10,42].

Whether EADs require $Ca^{2+}$ dynamics, or just $[Ca^{2+}]_i$ at an appropriate level, we propose that the dynamical mechanism is the same: twisted slow manifolds and canards. We have shown this here with the Luo-Rudy II model, and hope that future work from our group or others will succeed in testing this proposal in more biophysicallly complete cardiac myocyte models.

## Appendix A. Model equations.

**A.1. The full model and varied parameters.** The full 11-dimensional variant of the Luo-Rudy II model examined includes both electrical and intracellular $Ca^{2+}$ dynamics, but excludes potential spontaneous intracellular $Ca^{2+}$ release included in [31]:

$$
\begin{aligned}
C_m \frac{\mathrm{d}V}{\mathrm{d}t} &= -\sum I_{\text{ion}} + I_{\text{stim}} \\
\frac{\mathrm{d}m}{\mathrm{d}t} &= \frac{m_\infty - m}{\tau_m} \\
\frac{\mathrm{d}h}{\mathrm{d}t} &= \frac{h_\infty - h}{\tau_h} \\
\frac{\mathrm{d}j}{\mathrm{d}t} &= \frac{j_\infty - j}{\tau_j} \\
\frac{\mathrm{d}d}{\mathrm{d}t} &= \frac{d_\infty - d}{\tau_d} \\
\frac{\mathrm{d}f}{\mathrm{d}t} &= \frac{f_\infty - f}{\tau_f} \\
\frac{\mathrm{d}x}{\mathrm{d}t} &= \frac{x_\infty - x}{\tau_x}
\end{aligned}
\tag{A.1a}
$$

$$
\begin{aligned}
\frac{\mathrm{d}[\mathrm{Ca}]_{\mathrm{i}}}{\mathrm{d}t} &= b_i\left(J_{\text{in}}\frac{\mathrm{A_{cap}}}{2\mathrm{F}\ \mathrm{V_{myo}}} + J_{\text{rel}}\frac{\mathrm{V_{jsr}}}{\mathrm{V_{myo}}} + (J_{\text{leak}} - J_{\text{up}})\frac{\mathrm{V_{nsr}}}{\mathrm{V_{myo}}}\right) \\
\frac{\mathrm{d}[\mathrm{Ca}]_{\mathrm{jsr}}}{\mathrm{d}t} &= b_{sr}(J_{\text{tr}} - J_{\text{rel}}) \\
\frac{\mathrm{d}[\mathrm{Ca}]_{\mathrm{nsr}}}{\mathrm{d}t} &= -J_{\text{tr}}\frac{\mathrm{V_{jsr}}}{\mathrm{V_{nsr}}} - J_{\text{leak}} + J_{\text{up}}.
\end{aligned}
\tag{A.1b}
$$

Here, $I_{\text{ion}} = \{I_{\text{Na}}, I_{\text{Ca-L}}, I_{\text{K}}, I_{\text{K1}}, I_{\text{Kp}}, I_{\text{NaCa}}, I_{\text{NaK}}, I_{\text{nsCa}}, I_{\text{pCa}}, I_{\text{Cab}}, I_{\text{Nab}}\}$, which depend on the dynamic variables $(V, m, h, j, d, f, x, [Ca^{2+}]_i)$. The intracellular $Ca^{2+}$ fluxes $J_{\text{in}}$, $J_{\text{rel}}$, $J_{\text{leak}}$, $J_{\text{up}}$, and $J_{\text{tr}}$ depend on the dynamic variables ($[Ca^{2+}]_i$, $[Ca^{2+}]_{\text{jsr}}$, $[Ca^{2+}]_{\text{nsr}}$), with $J_{\text{rel}}$ also depending non-autonomously on time, $t$. Detailed model expressions and default parameter values can be found in the original article [31], from which variable, expression, and parameter names herein are duplicated.

Sections 2, 3, and 4 analyze the behavior of the clamped-$Ca^{2+}$ model (A.1a), in which $[Ca^{2+}]_i$, $[Ca^{2+}]_{jsr}$, and $[Ca^{2+}]_{nsr}$ are fixed and $[Ca^{2+}]_i$ alone enters (A.1a) as a parameter. Under this purely electrical 7-dimensional model variant, the maximum conductance parameters of $I_K$ ($\bar{G}_K$) and $I_{K1}$ ($\bar{G}_{K1}$) are varied alongside $[Ca^{2+}]_i$ to invoke EADs and examine solution behavior.

Section 5 then examines the full dynamic-$Ca^{2+}$ model through the imposition of $Ca^{2+}$ overload conditions. These conditions are simulated through the parameter choices enumerated in [31]: $[Ca^{2+}]_o = 3$ mmol/L, $[Na^+]_i = 15$ mmol/L, $P_{rel}$ (max $I_{Ca\text{-}L}$conductance) is increased 30%, and $\bar{G}_{rel}$($J_{rel}$ rate constant) $= 20$ ms$^{-1}$. In addition, the minimal dynamic-$Ca^{2+}$ model is analyzed under this same parameter regime, with $\bar{G}_{rel}$ varied to produce phase-3 EADs.

**A.2. Smooth approximation of piece-wise smooth gating functions.** To facilitate numerical computation, the piecewise continuous voltage-dependent gating functions formulated in [31] for the $I_{Na}$ conductance are replaced by smooth functions:

$$i_\infty = \frac{\alpha_i}{\alpha_i + \beta_i} \text{ for } i \in \{m, h, j\}$$

$$\alpha_m = \frac{0.32\,(V + 47.13)}{1 - e^{-0.1(V+47.13)}} \text{ and } \beta_m = 0.08e^{-V/11}$$

$$\alpha_h = 0.135e^{-(80+V)/6.8} \text{ and } \beta_h = \frac{1}{0.13(1 + e^{-(V+10.66)/11.1})}$$

$$\alpha_j = \frac{4.784 \times 10^{-7}}{e^{0.1045(-27.232+V)}} \text{ and } \beta_j = \frac{0.3e^{-2.535\times10^{-7}V}}{(1 + e^{-0.1(V+32)})}.$$

**A.3. Dynamic-$Ca^{2+}$ model reduction.** Figure 12 shows the simulated time courses of $[Ca^{2+}]_{jsr}$ (orange), $[Ca^{2+}]_{nsr}$ (purple), and $Ca^{2+}$ flux from the SR during $Ca^{2+}$-induced $Ca^{2+}$ release, $J_{rel}$ (blue), that accompany the voltage and $[Ca^{2+}]_i$ time courses shown in Fig. 7 (black curves). The vertical dashed line (red) denotes the time at which $I_{stim}$ is initiated and the time window in view terminates at 90% repolarization of the AP. The stimulus evokes a rapid pulse of $Ca^{2+}$ flux and the observed dynamics of $[Ca^{2+}]_{nsr}$ and $J_{rel}$ motivate a reduction of the dynamic-$Ca^{2+}$ model.

We estimated the timescale of $[Ca^{2+}]_{nsr}$ during an AP and found that even though $\tau_{[Ca^{2+}]_{nsr}} \approx 146$ ms is similar to $\bar{\tau}_x$, fixing $[Ca^{2+}]_{nsr}$ at its average value over the course of an AP produces EADs that are indistinguishable from those produced by the full model. Hence, we fix $[Ca^{2+}]_{nsr}$ at its average value ($\overline{[Ca^{2+}]_{nsr}} \approx 3.7082$ mM) and exclude the $[Ca^{2+}]_{nsr}$equation.

$Ca^{2+}$-induced $Ca^{2+}$ release from the SR produces a very short-lived $Ca^{2+}$ flux, $J_{rel}$, that vanishes just after the initiation of an AP. Since this is the only term that couples $[Ca^{2+}]_{jsr}$ to $[Ca^{2+}]_i$, the $[Ca^{2+}]_{jsr}$ and $[Ca^{2+}]_i$ differential equations are uncoupled throughout the remainder of the AP. Hence, we restrict our analysis to the window of time starting just after $J_{rel}$ has vanished, where the $[Ca^{2+}]_{jsr}$ differential equation is uncoupled from the rest of the system and can be excluded from analysis without affecting solution behavior.

As such, the minimal dynamic-$Ca^{2+}$ model is composed of the remaining differ-

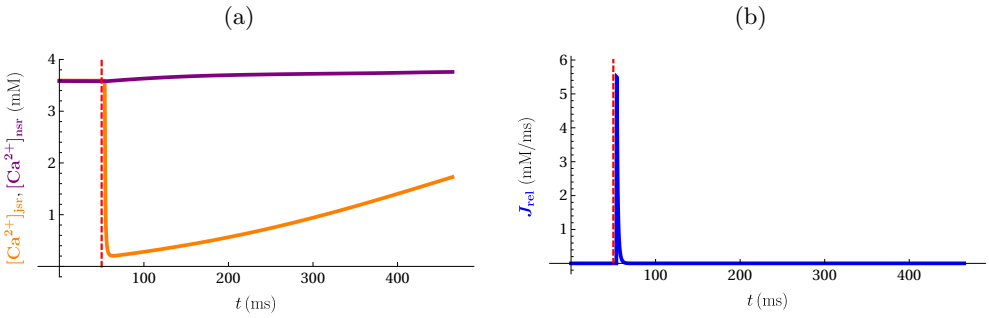


Fig. 12: **Time courses for $[Ca^{2+}]_{jsr}$, $[Ca^{2+}]_{nsr}$, and $J_{rel}$ during the AP with EADs produced by the dynamic-$Ca^{2+}$ model.** (a) $[Ca^{2+}]_{jsr}$ (orange) exhibits a fast downstroke subsequent to $I_{stim}$ pulse initiation (dashed, red) and slowly recovers over the duration of the AP. $[Ca^{2+}]_{nsr}$ (purple) exhibits slow growth over the course of the AP. (b) The pulse-like CICR flux, $J_{rel}$, which couples $[Ca^{2+}]_{jsr}$ to $[Ca^{2+}]_i$, immediately follows $I_{stim}$ initiation and vanishes for the remainder of the AP.

ential equations:

$$
\begin{aligned}
C_m \frac{\mathrm{d}V}{\mathrm{d}t} &= -\sum I_{\mathrm{ion}} \\
\frac{\mathrm{d}m}{\mathrm{d}t} &= \frac{m_\infty - m}{\tau_m} \\
\frac{\mathrm{d}h}{\mathrm{d}t} &= \frac{h_\infty - h}{\tau_h} \\
\frac{\mathrm{d}j}{\mathrm{d}t} &= \frac{j_\infty - j}{\tau_j} \\
\frac{\mathrm{d}d}{\mathrm{d}t} &= \frac{d_\infty - d}{\tau_d} \\
\frac{\mathrm{d}f}{\mathrm{d}t} &= \frac{f_\infty - f}{\tau_f} \\
\frac{\mathrm{d}x}{\mathrm{d}t} &= \frac{x_\infty - x}{\tau_x} \\
\frac{\mathrm{d}[\mathrm{Ca}]_i}{\mathrm{d}t} &= b_i \left[ J_{\mathrm{in}} \frac{\mathrm{A_{cap}}}{2\mathrm{F\ V_{myo}}} + (\bar{J}_{\mathrm{leak}} - J_{\mathrm{up}}) \frac{\mathrm{V_{nsr}}}{\mathrm{V_{myo}}} \right],
\end{aligned}
\tag{A.2}
$$

where $J_{rel}$ has been removed from the $[Ca^{2+}]_i$ equation, and $J_{leak}$, which is dependent only on $[Ca^{2+}]_{nsr}$, is now constant ($\bar{J}_{leak}$). Because these model reductions are valid for all times after the post-$I_{stim}$ $Ca^{2+}$ spike has decayed, $I_{stim}$ does not appear in the $V$-equation.

## Appendix B. Dimensional analysis of the $Ca^{2+}$-clamped model.

Dimensional analysis of (2.1) is performed by averaging the voltage-dependent time constants, $\tau_i$ for $i \in \{m, h, j, d, f, x\}$, over the duration of an AP to obtain mean timescales of the variables. We define the AP as beginning when the stimulus pulse is initiated and ending when the voltage reaches 90% repolarization. We then

non-dimensionalize the system via the rescalings:

$$V = c_V\, v, \quad t = c_t\, t_s, \quad I_\ell = c_I\, \tilde{I}_\ell, \tag{B.1}$$

for $\ell \in \{\text{Na, Ca-L, K, K1, Kp, NaCa, NaK, nsCa, pCa, Cab, Nab}\}$.

This results in the singularly perturbed dimensionless problem:

$$\begin{aligned}
\epsilon \frac{\mathrm{d}v}{\mathrm{d}t_s} &= -\sum \tilde{I}_{\text{ion}} \\
\frac{\epsilon}{r_m}\frac{\mathrm{d}m}{\mathrm{d}t_s} &= \frac{m_\infty - m}{\tilde{\tau}_m} \\
\frac{\epsilon}{r_h}\frac{\mathrm{d}h}{\mathrm{d}t_s} &= \frac{h_\infty - h}{\tilde{\tau}_h} \\
\frac{\epsilon}{r_j}\frac{\mathrm{d}j}{\mathrm{d}t_s} &= \frac{j_\infty - j}{\tilde{\tau}_j} \\
\frac{\epsilon}{r_d}\frac{\mathrm{d}d}{\mathrm{d}t_s} &= \frac{d_\infty - d}{\tilde{\tau}_d} \\
\frac{\mathrm{d}f}{\mathrm{d}t_s} &= \frac{f_\infty - f}{\tilde{\tau}_f} \\
\frac{\mathrm{d}x}{\mathrm{d}t_s} &= \frac{\bar{\tau}_f}{\bar{\tau}_x}\frac{x_\infty - x}{\tilde{\tau}_x}
\end{aligned} \tag{B.2}$$

where $c_V := 100$ mV, $c_t := \bar{\tau}_f \approx 30$ ms, and $c_I := \bar{g}_{\text{tot}} = 2$ mS/$\mu$F are chosen as characteristic voltage, timescale, and current amplitude, respectively. As such, $\epsilon := \frac{C_m}{\bar{g}_{\text{tot}}\,\bar{\tau}_f}$ ($\ll 1$)—the ratio of voltage and characteristic timescales—is a small perturbation parameter, $r_i := \frac{C_m}{\bar{g}_{\text{tot}}\,\bar{\tau}_i}$ for $i \in \{m, h, j, d\}$, $\bar{g}_{\text{tot}} \approx \sum_\ell g_\ell / n(\ell)$ for $\ell \in \{\text{Na, Ca-L, K, K1, Kp, NaCa, NaK, nsCa, pCa, Cab, Nab}\}$, and the right-hand sides of (B.2) are $\mathcal{O}(1)$ with respect to $\epsilon$.

## Appendix C. Computation of the slow manifolds and their continuations.

Here, we outline the numerical set-up used to compute the twisted slow manifolds. In Appendix C.1, we describe the adaptation required to track the slow manifolds when they are far from the folded node. With this adaptation, we then describe the computation of the attracting slow manifold in Appendix C.2 and the saddle slow manifold in Appendix C.3.

**C.1. Standardization of $\Sigma$.** Whereas the standard set-up chooses $\Sigma$ such that it contains the folded singularity, the significant movement of the twisted funnel under variation in $C_m$ and other parameters renders this choice inadequate. We choose $\Sigma$ in such a way that it tracks the movement of the twisted funnel. Let $p \in \mathbb{R}^d$ denote the vector of model parameters, which contains elements for $C_m$ and $\alpha_{I_{\text{K}},I_{\text{K1}}}$. For computation and visualization purposes, all slow manifolds are computed up to the $p$-dependent hyperplane

$$\Sigma := \{(V, m, h, j, d, f, x) \in \mathbb{R}^7 : a_p(f - f_p) + b_p(x - x_p) + e_p(V - V_p) = 0\} \tag{C.1}$$

and projected into $(f,\, x,\, V)$-space. Hence, the tuples $(a_p,\, b_p,\, e_p)$ and $(f_p,\, x_p,\, V_p)$ set the location of $\Sigma$ in phase space.

We first require that the coordinates $(f_p,\, x_p,\, V_p)$, which set the base point of $\Sigma$ in $(f, x, V)$ space, be the $f$, $x$ and $V$ coordinates of the turning point of the strong

canard. Then, ($a_p$, $b_p$, $e_p$) can be any set of points such that $\Sigma$ transversely intersects the continuations of the slow manifolds, $S^{a,+}_{C_m}$ and $S^{s}_{C_m}$. However, in practice some points work better than others. Through experimentation we found that setting ($a_p$, $b_p$, $e_p$) as the normal, in $(f, x, V)$-space, to the $f$, $x$, and $V$ component sub-vectors of the 2D unstable eigenspace of equilibrium $E_2$ allowed for robust computation across changes in $C_m$ and $\alpha_{I_{\mathrm{K}},I_{\mathrm{K1}}}$. Hence, $\Sigma$ is parallel to the 2D unstable eigenspace of $E_2$.

We reason that orienting $\Sigma$ this way works because $E_2$ is near enough in parameter space to the FSNII/singular Hopf bifurcation from which the canards arise and that the local twisting is still oriented with the 2D unstable manifold of $E_2$. Importantly however, the canard-induced rotational sectors are alone sufficient to explain EAD number; the computed continuations of the slow manifolds do not interact with this 2D unstable manifold in a way that requires more than the predictions from Fenichel and canard theory.

**C.2. 2-point boundary value problem set-up: attracting slow manifold computation.** Here, we outline the 2-point boundary value problem (2PBVP) set-up used in the computation of $S^{a,+}_{C_m}$of the clamped-$Ca^{2+}$ 2-slow variable problem. We have reprinted the model equations to define shorthand notation for the right-hand sides of the vector field:

$$
\begin{aligned}
\dot{V} &= -1/C_m \sum I_{\mathrm{ion}} := f_1(V, m, h, j, d, f, x) \\
\dot{m} &= \frac{m_\infty - m}{\tau_m} := f_2(V, m) \\
\dot{h} &= \frac{h_\infty - h}{\tau_h} := f_3(V, h) \\
\dot{j} &= \frac{j_\infty - j}{\tau_j} := f_4(V, j) \\
\dot{d} &= \frac{d_\infty - d}{\tau_d} := f_5(V, d) \\
\dot{f} &= \frac{f_\infty - f}{\tau_f} := s_1(V, f) \\
\dot{x} &= \frac{x_\infty - x}{\tau_x} := s_2(V, x).
\end{aligned}
\tag{C.2}
$$

The 2PBVP set-up can be denoted formally using the condensed notation:

$$
u = \begin{pmatrix} V \\ m \\ h \\ j \\ d \\ f \\ x \end{pmatrix}, \quad \dot{u} = T\,\boldsymbol{g}(u), \quad \begin{cases} u(0) \in \tilde{\Sigma}_0 \\ u(1) \in \tilde{\Sigma}_1. \end{cases}
\tag{C.3}
$$

where we follow the boundary condition notation in [13]. The solution integration time, $T$, which is treated as a free parameter is used to scale the time domain, $t \in [0, 1]$, and $\boldsymbol{g}$ is the vector field.

Defining a well-posed 2PBVP in 7D requires that the boundary conditions, $\tilde{\Sigma}_0$ and $\tilde{\Sigma}_1$, define codimension-$i$ and codimension-$k$ hypersurfaces, respectively, such that

$i+k=7$. As in [13], we compute the 2D attracting slow manifold continuation, $S^{a,+}_{C_m}$, by prescribing BCs:

$$\begin{cases} \tilde{\Sigma}_0 := \hat{\Sigma}_0 \cap \Sigma_0 = L^a \\ \tilde{\Sigma}_1 := \Sigma \end{cases} \tag{C.4}$$

where $L^a$ is a 1D curve on $S^{a,+}_0$ sufficiently far above the fold, $L$, and $\Sigma$ is our codimension-1 hyperplane (C.1) transverse to the flow. The condition

$$\hat{\Sigma}_0 := \{u \,|\, \dot{V}, \dot{m}, \dot{h}, \dot{j}, \dot{d} = 0 \tag{C.5}$$

restricts $L^a$ to lie along $S^{a,+}_0$ and the condition

$$\Sigma_0 := \{u \,|\, V = 30\} \tag{C.6}$$

ensures that $L^a$ is away from the fold.

Using a boundary value solver in tandem with pseudo-arclength homotopic continuation, facilitated by AUTO [8], we initialized the computations using a trivial segment–a single point ($T=0$)–which satisfies both sets of BCs. Manifolds were then grown as one parameter families of orbit segments through continuation in $T$.

**C.3. 2-point boundary value problem set-up: saddle slow manifold computation.** The 2PBVP set-up used in the computation of $S^s_{C_m}$ of the clamped-$Ca^{2+}$ problem differs meaningfully from that of $S^{a,+}_{C_m}$ and is described below. Again, we rewrite the problem using the condensed notation:

$$\dot{u} = T\,\boldsymbol{g}(u), \quad \begin{cases} u(0) \in \tilde{\Sigma}_0 \\ u(1) \in \tilde{\Sigma}_1. \end{cases} \tag{C.7}$$

For the computation of $S^s_{C_m}$ in $\mathbb{R}^7$, we generalize the approach from [13] for computing saddle slow manifolds in $\mathbb{R}^4$. The general prescribed BCs are as they are in [13]:

$$\begin{cases} \tilde{\Sigma}_0 := \hat{\Sigma}_0 \cap \Sigma_0 \\ \tilde{\Sigma}_1 := \hat{\Sigma}_1 \cap \Sigma_1. \end{cases} \tag{C.8}$$

Whereas in $\mathbb{R}^4$, both $\hat{\Sigma}_0$ and $\hat{\Sigma}_1$ are 3D submanifolds, in $\mathbb{R}^7$ $\hat{\Sigma}_0$ is 3D and $\hat{\Sigma}_0$ is 6D. Here, as in [13], $\hat{\Sigma}_0$ and $\hat{\Sigma}_1$ are chosen transverse to the stable and unstable manifolds of the saddle slow manifold $S^s_{C_m}$, respectively. This choice relies on these manifolds, in the vicinity of $S^s_{C_m}$, being smooth perturbations of the eigendirections of $S^s_0$ as equilibria of the fast subsystem. Hence, for our particular problem, $\hat{\Sigma}_0$ and $\hat{\Sigma}_1$ are defined as:

$$\begin{cases} \hat{\Sigma}_0 := \{u \,|\, \dot{m}, \dot{h}, \dot{j}, \dot{d} = 0\} = \{u \,|\, f_2, f_3, f_4, f_5 = 0\} \\ \hat{\Sigma}_1 := \{u \,|\, \dot{V} = 0\} = \{u \,|\, f_1 = 0\} \end{cases} \tag{C.9}$$

In contrast, $\Sigma_0$ and $\Sigma_1$ are 6D manifolds:

$$\begin{cases} \Sigma_0 := \Sigma \\ \Sigma_1 := \{u \,|\, V = -30\} \end{cases} \tag{C.10}$$

specified to ensure that orbit segments start on the defined cross-section and end far from the fold, $L$. The manifold, $S^s_{C_m}$, is then grown by starting from a trivial segment ($T = 0$) at which all BCs are satisfied and then continuing in $T$.

## Appendix D. 2-point boundary value problem set-up: computation of 1D maximal canard orbits and 2D maximal canard sets.

The procedure in [13] for the computation and continuation of 1D maximal canard orbits specifically addresses canards in (2,2)–fast-slow systems. For context in outlining the specifics of how these methods are extended for our computations, we review the key steps from [13].

With reference to the BC definitions in Appendix C, the recipe in [13] consists of two main steps. First, an orbit segment is computed in which $u(0) \in L^a$ and $u(1) \in \Sigma_1$, where the definitions for $L^a$ and $\Sigma_1$ are equivalent to those used to compute $S^{a,+}_{C_m}$ and $S^s_{C_m}$, respectively. Second, this orbit segment is continued by varying $u(0)$ along $L^a$ until the additional condition $u(1) \in \hat{\Sigma}_1$ ($\in S^s_{C_m}$) is satisfied; maximal canards correspond to isolated points along $L^a$. The resulting orbit segment, which transitions from $S^{a,+}_{C_m}$ to $S^s_{C_m}$ and remains on $S^s_{C_m}$ until termination, approximates a maximal canard.

In both the 2-slow and 3-slow variable settings, maximal canards can be computed as orbit segments which satisfy the general boundary conditions

$$\begin{cases} \tilde{\Sigma}_0 := \hat{\Sigma}_0 \cap \Sigma_0 = S^{a,+}_0 \cap \Sigma_0 \\ \tilde{\Sigma}_1 := \hat{\Sigma}_1 \cap \Sigma_1. \end{cases} \tag{D.1}$$

In both settings, $\Sigma_0$ and $\Sigma_1$ are codimension-1 hyperplanes, transverse to the flow, which ensure that orbit segments start and end, respectively, on either side of the fold set.

In the case of 2 slow variables, $S^{a,+}_0 \cap \Sigma_0$ is the 1D curve, $L^a$, where the presence of more than 2 fast variables is accounted for in the definition of $S^{a,+}_0$. Hence, in this setting, the existing two-step procedure from [13] is easily extended. However, in the case of 3 slow variables, $S^{a,+}_0 \cap \Sigma_0$ is a 2D plane; instead of corresponding to isolated points along the curve, $L^a$, maximal canards correspond to 1D loci along this 2D plane. How to locate and trace out such loci—associated to 1-parameter families of maximal canard orbit segments—is not addressed by the existing procedure.

Our approach to computing 2D sets of maximal canards, in analogy to [13], consist of 3 steps. First, we compute an orbit segment in which $u(0) \in \hat{L}^a$ and $u(1) \in \Sigma_1$. Here, $\hat{L}^a$ is a 1D curve along $S^{a,+}_0 \cap \Sigma_0$, chosen transverse to the 1D loci of maximal canard points; the definition of $\Sigma_1$ is equivalent to its definition in the computation of $S^s_{C_m}$. Second, we continue this computed orbit segment along $\hat{L}^a$ until $u(1) \in \hat{\Sigma}_1$ ($\in S^s_{C_m}$) is satisfied. The resulting orbit segment approximates a maximal canard within a 2D set. Third, we remove the constraint $u(0) \in \hat{L}^a$ and allow $u(0)$ to vary freely along the 2D plane, $S^{a,+}_0 \cap \Sigma_0$, requiring instead that $u(1) \in \hat{\Sigma}_1$ remains satisfied. This traces out a 2D manifold of maximal canard orbits.

For clarity, we provide the specific BCs used for maximal canard computation in the dynamic-$Ca^{2+}$ problem. For notational brevity, we augment system (C.2) with the $[Ca^{2+}]_i$ equation

$$\dot{[\mathrm{Ca}]}_\mathrm{i} = b_i\left(J_\mathrm{in}\frac{\mathrm{A_{cap}}}{2\mathrm{F}\ \mathrm{V_{myo}}} + (\bar{J}_\mathrm{leak} - J_\mathrm{up})\frac{\mathrm{V_{nsr}}}{\mathrm{V_{myo}}}\right) := s_3(V, d, f, [\mathrm{Ca}^{2+}]_\mathrm{i}). \tag{D.2}$$

and denote the 2PBVP set-up using the condensed notation:

$$u = \begin{pmatrix} V \\ m \\ h \\ j \\ d \\ f \\ x \\ [\mathrm{Ca}^{2+}]_{\mathrm{i}} \end{pmatrix}, \quad \dot{u} = T\,\boldsymbol{g}(u), \quad \begin{cases} u(0) \in \tilde{\Sigma}_0 \\ u(1) \in \tilde{\Sigma}_1. \end{cases} \tag{D.3}$$

For the initial homotopy step, we start with a solution segment which satisfies the BCs

$$\begin{cases} \tilde{\Sigma}_0 := S^{a,+}_{C_m} \cap \Sigma_0 \cap \Sigma_{\hat{L}^a} = \hat{L}^a \\ \tilde{\Sigma}_1 := \Sigma_1 \end{cases} \tag{D.4}$$

where

$$S^{a,+}_{C_m} := \{u \,|\, \dot{V}, \dot{m}, \dot{h}, \dot{j}, \dot{d} = 0\} = \{u \,|\, f_1, f_2, f_3, f_4, f_5 = 0\} \tag{D.5}$$

and

$$\begin{cases} \Sigma_0 := \{u \,|\, V = 30\} \\ \Sigma_{\hat{L}^a} := \{u \,|\, [\mathrm{Ca}^{2+}]_{\mathrm{i}} = 1.5(\mu\mathrm{M})\} \\ \Sigma_1 := \{u \,|\, V = -35\,\mathrm{mV}\}. \end{cases} \tag{D.6}$$

In the second step, varying $u(0)$ along $\hat{L}^a$ until $u(1) \in \hat{\Sigma}_1$ ($\in S^s_{C_m}$) is satisfied results in a maximal canard solution which obeys the BCs (D.1). Once here, the condition $u(0) \in \Sigma_{\hat{L}^a}$ is dropped and $u(1) \in S^s_{C_m}$ is retained to allow for computation of the located maximal canard set. Judicious choices for the initial location of $u(0) \in \hat{L}^a$ allow for different 2D maximal canard sets to be located and computed.

**Acknowledgments.** This work was partially funded by grant number DMS 1853342 to T. Vo and R. Bertram from the National Science Foundation

## REFERENCES

[1] D. S. Bailie, H. Inoue, S. Kaseda, J. Ben-David, and D. P. Zipes, *Magnesium suppression of early afterdepolarizations and ventricular tachyarrhythmias induced by cesium in dogs.*, Circulation, 77 (1988), pp. 1395–402, http://www.ncbi.nlm.nih.gov/pubmed/3370776.

[2] R. Barrio, M. A. Martínez, L. Pérez, and E. Pueyo, *Bifurcations and slow-fast analysis in a cardiac cell model for investigation of early afterdepolarizations*, Mathematics, 8 (2020), p. 880, https://doi.org/10.3390/math8060880.

[3] R. Bertram and J. E. Rubin, *Multi-timescale systems and fast-slow analysis*, Math. Biosci., 287 (2017), pp. 105–121, https://doi.org/10.1016/j.mbs.2016.07.003.

[4] N. Bögeholz, P. Pauls, B. K. Bauer, J. S. Schulte, D. G. Dechering, G. Frommeyer, U. Kirchhefer, J. I. Goldhaber, F. U. Müller, L. Eckardt, and C. Pott, *Suppression of early and late afterdepolarizations by heterozygous knockout of the $Na^+/Ca^{2+}$ exchanger in a murine model*, Circ. Arrhythm. Electrophysiol., 8 (2015), pp. 1210–1218, https://doi.org/10.1161/CIRCEP.115.002927.

[5] M. Brøns, M. Krupa, and M. Wechselberger, *Mixed mode oscillations due to the generalized canard phenomenon*, in Fields Inst. Commun., W. Nagata and N. S. Namarchehtvaya, eds., vol. 49, American Mathematical Society, Providence, Rhode Island, 2006, pp. 39–64, https://doi.org/10.1090/fic/049/03.

[6] P. F. Cranefield, A. L. Wit, and B. F. Hoffman, *Conduction of the cardiac impulse: III. Characteristics of very slow conduction.*, J. Gen. Physiol., 59 (1972), pp. 227–46, http://www.ncbi.nlm.nih.gov/pubmed/5058476.

[7] M. Desroches, B. Krauskopf, and H. M. Osinga, *The geometry of slow manifolds near a folded node*, SIAM J. Appl. Dyn. Syst., 7 (2008), pp. 1131–1162, https://doi.org/10.1137/070708810.

[8] E. J. Doedel, B. E. Oldeman, A. R. Champneys, F. Dercole, T. Fairgrieve, Y. Kuznetsov, R. Paffenroth, B. Sandstede, X. Wang, and C. Zhang, *AUTO-07P : Continuation and Bifurcation Software for Ordinary Differential Equations*, 2012.

[9] N. Fenichel, *Geometric singular perturbation theory for ordinary differential equations*, J. Differ. Equations, 31 (1979), pp. 53–98, https://doi.org/10.1016/0022-0396(79)90152-9.

[10] D. Guo, X. Zhao, Y. Wu, T. Liu, P. R. Kowey, and G.-X. Yan, *L-Type calcium current reactivation contributes to arrhythmogenesis associated with action potential triangulation*, J. Cardiovasc. Electr., 18 (2007), pp. 196–203, https://doi.org/10.1111/j.1540-8167.2006.00698.x.

[11] E. Harvey, V. Kirk, H. Osinga, J. Sneyd, and M. Wechselberger, *Understanding anomalous delays in a model of intracellular calcium dynamics*, Chaos, 20 (2010), p. 045104, moz-extension://6352bd84-90fc-454d-b951-c6ae2bb1e5cf/enhanced-reader.html?openApp&pdf=https%3A%2F%2Faip.scitation.org%2Fdoi%2Fpdf%2F10.1063%2F1.3523264.

[12] R. D. Harvey and R. E. Ten Eick, *Voltage-dependent block of cardiac inward-rectifying potassium current by monovalent cations*, J. Gen. Physiol., 94 (1989), pp. 349–361.

[13] C. R. Hasan, B. Krauskopf, and H. M. Osinga, *Saddle slow manifolds and canard orbits in $\mathbb{R}^4$ and application to the full Hodgkin-Huxley model*, J. Math. Neurosci., 8 (2018), https://doi.org/10.1186/s13408-018-0060-1.

[14] B. Horvath, T. Banyasz, Z. Jian, B. Hegyi, K. C. Kistamas, P. P. Nanasi, L. T. Izu, Y. Chen-Izu, and Y. Edu, *Dynamics of the Late $Na^+$ current during cardiac action potential and its contribution to afterdepolarizations*, J. Mol. Cell. Cardiol., 64 (2013), https://doi.org/10.1016/j.yjmcc.2013.08.010.

[15] B. Horváth, B. Hegyi, K. Kistamás, K. Váczi, T. Bányász, J. Magyar, N. Szentandrássy, and P. P. Nánási, *Cytosolic calcium changes affect the incidence of early afterdepolarizations in canine ventricular myocytes*, Can. J. Physiol. Pharm., 93 (2015), pp. 527–534, https://doi.org/10.1139/cjpp-2014-0511.

[16] C. T. January and J. M. Riddle, *Early afterdepolarizations: mechanism of induction and block. A role for L-type $Ca^{2+}$ current.*, Circ. Res., 64 (1989), pp. 977–90, https://doi.org/10.1161/01.RES.64.5.977.

[17] C. T. January, J. M. Riddle, and J. J. Salata, *A model for early afterdepolarizations: induction with the Ca2+ channel agonist Bay K 8644.*, Circ. Res., 62 (1988), pp. 563–71, https://doi.org/10.1161/01.RES.62.3.563.

[18] C. K. R. T. Jones, *Geometric singular perturbation theory*, in Dynamical Systems, Springer, Berlin, 1995, pp. 44–118, https://doi.org/10.1007/BFb0095239.

[19] S. Kettlewell, P. Saxena, J. Dempster, M. A. Colman, R. C. Myles, G. L. Smith, and A. J. Workman, *Dynamic clamping human and rabbit atrial calcium current: narrowing $I_{CaL}$ window abolishes early afterdepolarizations*, J. Physiol., 597 (2019), pp. 3619–3638, https://doi.org/10.1113/JP277827.

[20] J. J. Kim, J. Němec, Q. Li, and G. Salama, *Synchronous Systolic Subcellular $Ca^{2+}$-Elevations Underlie Ventricular Arrhythmia in Drug-Induced Long QT Type 2*, Circ. Arrhythm. Electrophysiol., 8 (2015), pp. 703–712, https://doi.org/10.1161/CIRCEP.114.002214.

[21] J. J. Kim, J. Němec, R. Papp, R. Strongin, J. J. Abramson, and G. Salama, *Bradycardia alters $Ca^{2+}$ dynamics enhancing dispersion of repolarization and arrhythmia risk*, Am. J. Physiol., 304 (2013), p. H848, https://doi.org/10.1152/AJPHEART.00787.2012.

[22] J. Kimrey, T. Vo, and R. Bertram, *Big Ducks in the Heart: Canard Analysis Can Explain Large Early Afterdepolarizations in Cardiomyocytes*, SIAM J. Appl. Dyn. Syst., 19 (2020), pp. 1701–1735, https://doi.org/10.1137/19m1300777.

[23] J. Kimrey, T. Vo, and R. Bertram, *Canard analysis reveals why a large $Ca^{2+}$ window current promotes early afterdepolarizations in cardiac myocytes*, PLOS Comput. Biol., 16 (2020), p. e1008341, https://doi.org/10.1371/journal.pcbi.1008341.

[24] M. Krupa and P. Szmolyan, *Extending geometric singular perturbation theory to nonhyperbolic points - fold and canard points in two dimensions*, SIAM J. Math. Anal., 33 (2001), pp. 286–314, https://doi.org/10.1137/S0036141099360919.

[25] P. Kügler, *Early afterdepolarizations with growing amplitudes via delayed subcritical hopf bifurcations and unstable manifolds of saddle foci in cardiac action potential dynamics*,

PLoS ONE, 11 (2017), p. e0151178, https://doi.org/10.1371/journal.pone.0151178.
[26] P. Kügler, A. H. Erhardt, and M. A. K. Bulelzai, *Early afterdepolarizations in cardiac action potentials as mixed mode oscillations due to a folded node singularity*, PLoS ONE, 13 (2018), p. e0209498, https://doi.org/10.1371/journal.pone.0209498.
[27] Y. Kurata, K. Tsumoto, K. Hayashi, I. Hisatome, Y. Kuda, and M. Tanida, *Multiple dynamical mechanisms of phase-2 early afterdepolarizations in a human ventricular myocyte model: involvement of spontaneous SR $Ca^{2+}$ release*, Front. Physiol., 10 (2020), p. 1545, https://doi.org/10.3389/fphys.2019.01545, www.frontiersin.org.
[28] J. Kuusela, K. Larsson, D. Shah, C. Prajapati, and K. Aalto-Setälä, *Low extracellular potassium prolongs repolarization and evokes early afterdepolarization in human induced pluripotent stem cell-derived cardiomyocytes.*, Biol. Open, 6 (2017), pp. 777–784, https://doi.org/10.1242/bio.024216.
[29] Y. X. Li and J. Rinzel, *Equations for InsP3 receptor-mediated $[Ca^{2+}]_i$ oscillations derived from a detailed kinetic model: A Hodgkin-Huxley like formalism*, J. Theor. Biol., 166 (1994), pp. 461–473, https://doi.org/10.1006/jtbi.1994.1041.
[30] C.-H. Luo and Y. Rudy, *A model of the ventricular cardiac action potential*, Circ. Res., 68 (1991), pp. 1501–1526, https://doi.org/10.1161/01.RES.68.6.1501.
[31] C.-H. Luo and Y. Rudy, *A dynamic model of the cardiac ventricular action potential. I. Simulations of ionic currents and concentration changes.*, Circ. Res., 74 (1994), pp. 1071–96, https://doi.org/10.1161/01.RES.74.6.1071.
[32] C.-H. Luo and Y. Rudy, *A dynamic model of the cardiac ventricular action potential II. Afterdepolarizations, triggered activity, and potentiation*, Circ. Res., 74 (1994), pp. 1097–113.
[33] R. V. Madhvani, M. Angelini, Y. Xie, A. Pantazis, S. Suriany, N. P. Borgstrom, A. Garfinkel, Z. Qu, J. N. Weiss, and R. Olcese, *Targeting the late component of the cardiac L-type $Ca^{2+}$ current to suppress early afterdepolarizations*, J. Gen. Physiol., 145 (2015), pp. 395–404, https://doi.org/10.1085/jgp.201411288.
[34] R. V. Madhvani, Y. Xie, A. Pantazis, A. Garfinkel, Z. Qu, J. N. Weiss, and R. Olcese, *Shaping a new $Ca^{2+}$ conductance to suppress early afterdepolarizations in cardiac myocytes*, J. Physiol., 589 (2011), pp. 6081–6092, https://doi.org/10.1113/jphysiol.2011.219600.
[35] E. Marban, S. W. Robinson, and W. G. Wier, *Mechanisms of arrhythmogenic delayed and early afterdepolarizations in ferret ventricular muscle.*, The Journal of Clinical Investigation, 78 (1986), pp. 1185–92, https://doi.org/10.1172/JCI112701.
[36] C. F. Meier and B. G. Katzung, *Cesium blockade of delayed outward currents and electrically induced pacemaker activity in mammalian ventricular myocardium*, J. Gen. Physiol., 77 (1981), pp. 531–547.
[37] L. Nalos, R. Varkevisser, M. K. Jonsson, M. J. Houtman, J. D. Beekman, R. Van Der Nagel, M. B. Thomsen, G. Duker, P. Sartipy, T. P. De Boer, M. Peschar, M. B. Rook, T. A. Van Veen, M. A. Van Der Heyden, and M. A. Vos, *Comparison of the $I_{Kr}$ blockers moxifloxacin, dofetilide and E-4031 in five screening models of pro-arrhythmia reveals lack of specificity of isolated cardiomyocytes*, Brit. J. Pharmacol., 165 (2012), pp. 467–478, https://doi.org/10.1111/j.1476-5381.2011.01558.x.
[38] T. O'Hara, L. Virág, A. Varró, and Y. Rudy, *Simulation of the Undiseased Human Cardiac Ventricular Action Potential: Model Formulation and Experimental Validation*, PLOS Comput. Biol., 7 (2011), p. 1002061, https://doi.org/10.1371/journal.pcbi.1002061.
[39] O. E. Osadchii, *Mechanisms of hypokalemia-induced ventricular arrhythmogenicity*, Fund. Clin. Pharmacol., 24 (2010), pp. 547–559, https://doi.org/10.1111/j.1472-8206.2010.00835.x.
[40] A. Pezhouman, N. Singh, Z. Song, M. Nivala, A. Eskandari, H. Cao, A. Bapat, C. Y. Ko, T. P. Nguyen, Z. Qu, H. S. Karagueuzian, and J. N. Weiss, *Molecular basis of hypokalemia-induced ventricular fibrillation*, Circulation, 132 (2015), pp. 1528–1537, https://doi.org/10.1161/CIRCULATIONAHA.115.016217.
[41] S. G. Priori and P. B. Corr, *Mechanisms underlying early and delayed afterdepolarizations induced by catecholamines*, Am. J. Physiol., 256 (1990), pp. H1796–H1805, https://doi.org/10.1152/ajpheart.1990.258.6.h1796.
[42] Z. Qu, L.-H. Xie, R. Olcese, H. S. Karagueuzian, P.-S. Chen, A. Garfinkel, and J. N. Weiss, *Early afterdepolarizations in cardiac myocytes: beyond reduced repolarization reserve.*, Cardiovasc. Res., 99 (2013), pp. 6–15, https://doi.org/10.1093/cvr/cvt104.
[43] D. M. Roden, *Taking the "Idio" out of "Idiosyncratic": predicting Torsades de Pointes*, PACE, 21 (1998), pp. 1029–1034, https://doi.org/10.1111/j.1540-8159.1998.tb00148.x.
[44] J. Rubin and M. Wechselberger, *Giant squid-hidden canard: The 3D geometry of the*

*Hodgkin-Huxley model*, Biol. Cybern., 97 (2007), pp. 5–32, https://doi.org/10.1007/s00422-007-0153-5.

[45] D. Sato, L.-H. Xie, T. P. Nguyen, J. N. Weiss, and Z. Qu, *Irregularly appearing early afterdepolarizations in cardiac myocytes: random fluctuations or dynamical chaos?*, Biophys. J., 99 (2010), pp. 765–773, https://doi.org/10.1016/J.BPJ.2010.05.019.

[46] C. I. Spencer and J. S. K. Sham, *Effects of $Na^+$ /$Ca^{2+}$ exchange induced by SR $Ca^{2+}$ release on action potentials and afterdepolarizations in guinea pig ventricular myocytes*, Am. J. Physiol., 285 (2003), pp. H2552–H2562, https://doi.org/10.1152/ajpheart.00274.2003.

[47] C. R. Studenik, Z. Zhou, and C. T. January, *Differences in action potential and early afterdepolarization properties in LQT2 and LQT3 models of long QT syndrome*, Brit. J. Pharmacol., 132 (2001), pp. 85–92, www.nature.com/bjp.

[48] P. Szmolyan and M. Wechselberger, *Canards in $\mathbb{R}^3$*, J. Differ. Equations, 177 (2001), pp. 419–453, https://doi.org/10.1006/jdeq.2001.4001, https://arxiv.org/abs/NIHMS150003.

[49] K. H. Ten Tusscher, D. Noble, P. J. Noble, and A. V. Panfilov, *A model for human ventricular tissue*, Am. J. Physiol., 286 (2004), pp. H1573–89, https://doi.org/10.1152/ajpheart.00794.2003.

[50] J. Tomek, A. Bueno-Orovio, E. Passini, X. Zhou, A. Minchole, O. Britton, C. Bartolucci, S. Severi, A. Shrier, L. Virag, A. Varro, and B. Rodriguez, *Development, calibration, and validation of a novel human ventricular myocyte model in health, disease, and drug block*, eLife, 8 (2019), p. e48890, https://doi.org/10.7554/eLife.48890.

[51] D. X. Tran, D. Sato, A. Yochelis, J. N. Weiss, A. Garfinkel, and Z. Qu, *Bifurcation and chaos in a model of cardiac early afterdepolarizations*, Phys. Rev. Lett., 102 (2009), p. 258103, https://doi.org/10.1103/PhysRevLett.102.258103.

[52] G. Tse, *Mechanisms of cardiac arrhythmias.*, J. Arrhythmia, 32 (2016), pp. 75–81, https://doi.org/10.1016/j.joa.2015.11.003.

[53] T. Vo and R. Bertram, *Why pacing frequency affects the production of early afterdepolarizations in cardiomyocytes: An explanation revealed by slow-fast analysis of a minimal model*, Phys. Rev. E, 99 (2019), https://doi.org/10.1103/PhysRevE.99.052205.

[54] M. Wechselberger, *Existence and bifurcation of canards in $\mathbb{R}^3$ in the case of a folded node*, SIAM J. Appl. Dyn. Syst., 4 (2005), pp. 101–139, https://doi.org/10.1137/030601995.

[55] M. Wechselberger, *Apropos canards*, Trans. Amer. Math. Soc, 364 (2012), pp. 3289–3309.

[56] J. N. Weiss, A. Garfinkel, H. S. Karagueuzian, P.-S. Chen, and Z. Qu, *Early afterdepolarizations and cardiac arrhythmias.*, Heart Rhythm, 7 (2010), pp. 1891–9, https://doi.org/10.1016/j.hrthm.2010.09.017.

[57] J. N. Weiss, Z. Qu, and K. Shivkumar, *Electrophysiology of hypokalemia and hyperkalemia.*, Circ. Arrhythm. Electrophysiol., 10 (2017), https://doi.org/10.1161/CIRCEP.116.004667.

[58] D. Wilson, B. Ermentrout, J. Němec, and G. Salama, *A model of cardiac ryanodine receptor gating predicts experimental $Ca^{2+}$-dynamics and $Ca^{2+}$-triggered arrhythmia in the long QT syndrome*, Chaos, 27 (2017), https://doi.org/10.1063/1.5000711.

[59] G.-X. Yan, Y. Wu, T. Liu, J. Wang, R. A. Marinchak, and P. R. Kowey, *Phase 2 early afterdepolarization as a trigger of polymorphic ventricular tachycardia in acquired long-QT Syndrome: direct evidence from intracellular recordings in the intact left ventricular wall*, Circulation, 103 (2001), pp. 2851–2856.

[60] J. A. Yao and G. N. Tseng, *Azimilide (NE-10064) can prolong or shorten the action potential duration in canine ventricular myocytes: Dependence on blockade of K, Ca, and Na channels*, J. Cardiovasc. Electr., 8 (1997), pp. 184–198, https://doi.org/10.1111/j.1540-8167.1997.tb00780.x.

[61] Z. Zhao, H. Wen, N. Fefelova, C. Allen, A. Baba, T. Matsuda, L.-H. Xie, and L.-h. Xie, *Revisiting the ionic mechanisms of early afterdepolarizations in cardiomyocytes: predominant by Ca waves or Ca currents?*, Am. J. Physiol., 302 (2012), pp. H1636–H1644, https://doi.org/10.1152/ajpheart.00742.2011.-Early.